Characterizing meso- to submesoscale features in the South China Sea

Hongyang Lin[a,b], Zhiyu Liu[a,*], Jianyu Hu[a,b,*], Dimitris Menemenlis[c], Yongxiang Huang[a,d]

[a] State Key Laboratory of Marine Environmental Science, and Department of Physical Oceanography, College of Ocean and Earth Sciences, Xiamen University, Xiamen, Fujian 361102, China
[b] Southern Marine Science and Engineering Guangdong Laboratory (Zhuhai), Zhuhai, Guangdong 519000, China
[c] Jet Propulsion Laboratory, California Institute of Technology, Pasadena, CA, USA
[d] Fujian Engineering Research Center for Ocean Remote Sensing Big Data, Xiamen, Fujian 361102, China

ARTICLE INFO

ABSTRACT

In this study the mesoscale and submesoscale features in the South China Sea (SCS) are characterized based on a submesoscale-permitting numerical simulation (MITgcm llc4320) with nominal horizontal grid spacing of $1/48°$ (~2.2 km in the SCS). The simulation includes tidal forcing, which is particularly crucial in the SCS where tides play a key role in many aspects of regional dynamics. Evaluation against observations demonstrates that the simulation is capable of reproducing a wide spectrum of dynamical features in the SCS. The simulation is then used to characterize meso- to submesoscale features in the SCS and the key findings are summarized as follows: (i) the SCS is rich in submesoscale features (e.g., vortices, filaments), which undergo significant seasonal variations in many regions; (ii) there is a clear dominance of positive surface relative vorticity (ζ) in most regions of the SCS presumably due to the centrifugal instability, but large negative ζ also emerges in areas with strong flow-topography interactions; (iii) the vertical motions in the upper SCS are dominated by tidal modulations with strong vertical velocities up to 0.01 m s^{-1}, about an order of magnitude larger than those due to the quasi-balanced sub-inertial motions; and (iv) both the wintertime and summertime horizontal wavenumber spectra of kinetic energy scale roughly as k^{-2} (with k being the horizontal wavenumber) for wavelengths below 100 km. In addition, four key regions are highlighted with distinctive characteristics of submesoscale turbulence, including the northern SCS, Luzon Strait, the SCS western boundary current region in winter, and east of Vietnam in summer. A number of model deficiencies are noted, along with suggestions for improving model accuracy in order to better characterize the local submesoscale features as well as the underlying dynamics.

1. Introduction

Studies on the mesoscale flow field and small-scale processes in the ocean have been intensively carried out for decades. Mesoscale processes are primarily in geostrophic (and hydrostatic) balance, encompass the largest part of oceanic kinetic energy (Ferrari and Wunsch, 2009), and are characterized by an overall inverse energy cascade (Charney, 1971). Small-scale three-dimensional oceanic turbulence is widely recognized for its role in diabatic destratification (diapycnal mixing) and kinetic energy dissipation. The submesoscale turbulence, with a spatial scale of about 1–20 km between the mesoscale and small scale, and a time scale near the local inertial period, has nevertheless not been understood adequately to date. This is due to challenges in both numerical modeling and observations at this intermediate scale. From the viewpoint of energy cascade, submesoscale turbulence is expected to seamlessly link mesoscales and small scales and hence to close the oceanic energy pathway from the forcing to dissipative scales. In addition, the submesoscale is often accompanied by much larger vertical velocities, typically by one-to-two orders of magnitude, than those induced by mesoscale processes (Thomas et al., 2008). This highlights submesoscale turbulence as an efficient medium communicating the upper and interior ocean with biophysical properties (Mahadevan, 2016).

A couple of mechanisms have been proposed for the generation of submesoscale turbulence (McWilliams, 2016). The first mechanism is mixed-layer instability (Haine and Marshall, 1998; Boccaletti et al., 2007). Baroclinic instability developed in the mixed layer converts available potential energy to kinetic energy at a scale close to the mixed-layer deformation radius, Nh/f, which is of order 1 km given typical values of the buoyancy frequency N (10^{-3} s^{-1}), mixed-layer

depth h (100 m), and the Coriolis parameter f (10^{-4} s^{-1}). As such perturbations grow to finite amplitude, there will be exchange of kinetic energy between differing scales due to nonlinear advective interactions. As noted by Callies et al. (2015), an inverse energy cascade subsequently occurs throughout the entire mixed layer at scales between the mesoscale and the mixed-layer deformation radius because the Earth's rotation becomes important at these scales. The second mechanism is strain-induced frontogenesis (Lapeyre and Klein, 2006; Capet et al., 2008b). Submesoscale frontal features (e.g., sharp edges or filaments) are often seen in vorticity or buoyancy fields, many of which are caused by frontogenesis. Such regions are associated with relatively high strain rates that primarily arise from mesoscale flows. The evolution of the front is normally accompanied by a cross-frontal secondary circulation that tends to slump the tilting isopycnals, leading to restratification in the frontal region. There are a few more mechanisms that could excite submesoscale turbulence (Thomas et al., 2008). For example, mesoscale flows experiencing buoyancy loss or down-front winds could lead to the onset of submesoscale instabilities. Another example is a flow that passes topographic obstacles and triggers submesoscale vortices and filaments in the wakes of these obstacles.

Wavenumber spectra of horizontal kinetic energy or tracers in the upper mixed layer have commonly been evaluated to examine how the variance is contributed by variability at different length scales, including the submesoscale. The analysis has been based on satellite altimetry observations (e.g., Stammer, 1997; Le Traon et al., 2008), numerical simulations (e.g., Capet et al., 2008a; Sasaki and Klein, 2012), *in situ* measurements (e.g., Wang et al., 2010; Callies and Ferrari, 2013; Timmermans and Winsor, 2013) or a combination of these sources (e.g., Richman et al., 2012; Rocha et al., 2016a). One important but disputed issue is whether submesoscale dynamics can be described by the interior quasi-geostrophic (QG) turbulence theory (Charney, 1971), the surface quasi-geostrophic (SQG) theory (Blumen, 1978), or the internal-wave continuum (Garrett and Munk, 1972). The QG theory, predicting a k^{-3} power law (with k being horizontal wavenumber) in horizontal wavenumber spectra, is usually used to characterize two-dimensional mesoscale turbulence. The SQG theory, predicting a $k^{-5/3}$ spectral scaling, is applicable to upper ocean dynamics that is driven by density evolution at the sea surface (Le Traon et al., 2008). The internal-wave continuum, predicting a k^{-2} spectral scaling (e.g., Callies and Ferrari, 2013), is a useful model to characterize internal gravity wave variability. Although, as pointed out by previous investigators, the scaling itself does not definitely distinguish the underlying dynamics (Timmermans and Winsor, 2013; Callies et al., 2015), it is a useful tool for examining submesoscale variability.

The South China Sea (SCS) is a dynamically important marginal sea of the North Pacific. It is a good epitome of the open ocean with well-defined continental shelf, shelf break, and the central deep basin (Fig. 1). Submesoscale studies in the SCS are still at an early stage and most of them are based on numerical simulations (e.g., Liu et al., 2010; Dong and Zhong, 2018). One of the most essential drawbacks of previous simulations for the SCS (and for many other regions of the world ocean) is the exclusion of tides. This is an especially problematic issue for the SCS because the Luzon Strait is the most energetic region in the world ocean in terms of internal tide generation (Alford et al., 2015) and the SCS (in particular the northern SCS) is significantly affected by subsequent propagation, degeneration, and dissipation of internal tides. Another issue is that the submesoscale-permitting (normally achieved through nesting) model domains in previous studies are restricted to limited regions, such as the northern SCS (Liu et al., 2010; Zhong et al., 2017; Dong and Zhong, 2018; Li et al., 2019). This study aims to characterize the submesoscale turbulence in the entire SCS based on output from a global submesoscale-permitting, primitive-equation-based numerical simulation. The unique feature of this simulation compared with previous simulations is that it resolves internal tides well and even admits some smaller-scale processes, allowing us to characterize more realistic features of mesoscale and submesoscale
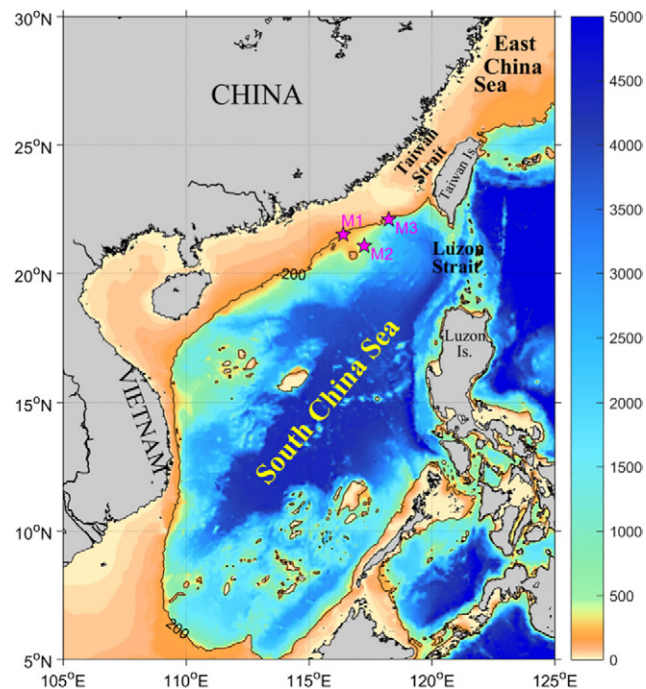
Fig. 1. Map of the South China Sea and adjacent regions. The color shading shows the bathymetry with the black contours denoting the coastline and the 200-m isobath. The magenta pentagrams show the location of three moorings, which provided the measurements used to estimate the observed velocity spectra shown in Fig. 4. (For interpretation of the references to color in this figure legend, the reader is referred to the web version of this article.)

processes in the SCS.

The manuscript is structured as follows. Section 2 introduces the data and the model used in this study. The model output is evaluated using satellite and mooring observations in Section 3, demonstrating the model's capability to reproduce many phenomena on a variety of spatiotemporal scales. Section 4 describes the general submesoscale features in the SCS based on model output, with detailed structures in several key regions highlighted in Section 5. Section 6 includes a summary and discussion.

2. Data and model

This section briefly introduces the submesoscale-permitting model used in the present study as well as the satellite and mooring data used to evaluate the model output.

2.1. Data

Satellite data. Satellite data of the sea level and sea surface temperature (SST) are used in this study. Both gridded (constructed from multiple altimetry missions) and along-track sea level data are used and obtained from the Copernicus Marine Environment Monitoring Service (CMEMS; http://marine.copernicus.eu/). The gridded absolute dynamic topography (with a grid spacing of 1/4° and daily interval) data are used to evaluate the simulated sea level. The Cryosat-2 along-track sea level data are also used to estimate the wavenumber spectra of the sea surface height (SSH) as this altimeter covers a contemporaneous period with the numerical simulations. The along-track sea level data have a spatial spacing of $\sim$ 6.4 km and are interpolated to have a spatial interval of 6 km prior to the spectral calculations. The SST data used in this study are collected by the Modis-Terra satellite and distributed by the Ocean Color website (https://oceancolor.gsfc.nasa.gov/). We use a monthly gridded SST product provided on a grid with 4-km spacing to compare with the simulated mean SST field.

Reanalysis data. The reanalysis dataset is the GLORYS12V1, also obtained from CMEMS (GLOBAL_REANALYSIS_PHY_001_030). The reanalysis data have a grid spacing of 1/12° and a time interval of one day. The reanalysis is based on NEMO (Nucleus for European Modelling of the Ocean) with intense data assimilation.

Mooring data. There are three moorings located roughly at the shelf break of the northern SCS (magenta pentagrams in Fig. 1). The moorings were deployed in April 2014 and recovered in October 2014. Each mooring has an upward-looking ADCP (acoustic Doppler current profiler) mounted at a depth of ~ 250 m for M1 and ~ 500 m for M2 and M3. The time interval of the current measurements is 10 min for M1 and 1 h for M2 and M3. The currents data from the moorings will be used to evaluate the velocity frequency spectra obtained from the model.

2.2. Model (MITgcm llc4320)

The model output used in this study is based on the Massachusetts Institute of Technology general circulation model (MITgcm) (Marshall et al., 1997). We use a simulation called llc4320, which has nominal horizontal grid spacing of 1/48° globally (~2.2 km in the SCS). Output snapshots are available at an hourly time interval and span 14 months, from September 2011 to November 2012. The MITgcm simulation was forced by six-hourly atmospheric fields from the 0.14° European Center for Medium Range Weather Forecasts (ECMWF) operational atmospheric reanalysis (ECMWF, 2011). The ECMWF fields are converted to surface fluxes using the Large and Yeager (2004) versions of the bulk formulae. The MITgcm simulation was also forced by ECMWF atmospheric pressure loading and by lunar and solar tidal potential applied as additional surface pressure. As mentioned by Rocha et al. (2016b), there is significant transfer from tide to internal-wave energy and the latter has projections onto mesoscale and submesoscale motions. Therefore, it is crucial to use ocean model simulations that include tidal forcing to investigate submesoscale processes in the tidally energetic SCS. This is a distinguishing feature of the present study compared to previous studies. Another novelty is that although the llc4320 simulation has been used in many other regions of the global ocean, e.g., Drake Passage (Rocha et al., 2016a) and Kuroshio Extension (Rocha et al., 2016b), this is the first study that examines the llc4320 simulation in the SCS. In the following section, we evaluate the llc4320 model output using the above-mentioned satellite and mooring data, before using the model results to characterize regional submesoscale features.

3. Evaluation of the llc4320 simulation in the SCS

We evaluate the performance of the MITgcm llc4320 simulation in the SCS by comparing (i) the simulated, de-tided sea level with altimeter observations, (ii) the simulated SST and sea surface salinity (SSS) with the satellite and reanalysis data, (iii) the velocity frequency spectra with mooring observations, and (iv) the co-tidal charts with previous studies.

3.1. Sea level

The mean and standard deviation of simulated SSH are compared with the gridded absolute dynamic topography from satellite observations. As tidal signals have been filtered in the gridded satellite SSH data, tidal modulations in the simulated SSH have been removed using the T_Tide package (Pawlowicz et al., 2002) prior to the calculation of the first two moments. It is shown that the llc4320 simulation can generally reproduce the mean sea level field (Fig. 2a-b) in terms of both large-scale circulation (e.g., the cyclonic circulation in the northern SCS basin, the overall Kuroshio path) and mesoscale features (e.g., the Kuroshio loop at the Luzon Strait).

The standard deviation of observed and simulated SSH is also qualitatively similar, for example the relatively high values southwest

of Taiwan Island and southeast of Vietnam. Note that the SSH standard deviation calculated using daily-averaged model output (not shown) is similar to Fig. 2d, which is based on hourly output and tide removal using the T_Tide package. Although fully explaining the model-data SSH differences is beyond the scope of this study, we note that there are differences in data processing that may explain some of the observed standard-deviation differences. Firstly, the model includes atmospheric pressure forcing, which is removed via inverse barometer correction in the CMEMS SSH product. Secondly, the removal of tides via T_Tide for the model is not equivalent to the way tides are removed from the CMEMS SSH product. In particular, T_Tide or daily averaging will tend to reduce the internal-tide signals at the surface while the CMEMS correction does not. Thirdly, some residual tidal errors will be aliased in the CMEMS SSH. Finally, the underestimation could also be due to the fact that the model is run for only one seasonal cycle, and it is possible that the state equilibrium has not been fully achieved.

3.2. SST and SSS

The simulated mean SST field is remarkably similar to the mean SST obtained from satellite observations and reanalysis (Fig. 3a-c). In addition to the southeastward gradient of mean SST in the SCS deep basin, the simulation is also able to reproduce the cold water patch along the Chinese coast. The simulated SSS could only be compared to the reanalysis since the spatial resolution of satellite observed SSS is too low. The basin-scale characteristics of the observed and simulated mean SSS fields are similar. However, the model is incapable of reproducing the low-salinity strip in the nearshore region (Fig. 3d-e) due to the over-simplified representation of river runoff in the llc4320 simulation, which used time-mean runoff forcing processed by Stammer et al. (2004) based on Large and Nurser (2001). For example, the inaccurate representation of the Yangtze River discharge affects the path and salinity of the China Coast Current in winter, which leads to the salinity bias seen in the nearshore area.

3.3. Velocity frequency spectra

Comparisons of spatial patterns have shown reasonably good agreement. Now we compare the temporal variability of the observation and simulation by examining the velocity spectra at the three mooring sites (see Fig. 1 for locations). It is evident that the simulated velocity spectra agree fairly well with the observed spectra at super-inertial frequencies for all three locations (Fig. 4). To quantify, we calculate the ratios of the simulated velocity spectra over the observed spectra, and the median values of ratios at sub- and super-inertial frequencies, respectively. The model generally underestimates the observed sub-inertial variability by a factor of about two. It is expected that the simulated and observed velocity spectra have lesser agreement at sub-inertial frequencies because the model simulation (September 2011 to November 2012) and mooring measurements (April-October 2014) are not contemporaneous. At the super-inertial range, the median values of the simulated/observed ratios are around 1.7 for 50-m velocities at all the three locations; ratios for 200-m velocities are slightly diverse: the median ratio is 3.1 at station M1, suggesting an overestimation, but the median ratio is 0.8 at stations M2 and M3, suggesting an underestimation. Overall, the agreement at super-inertial frequencies is better compared to sub-inertial frequencies as most of the variability is associated with tidal motions, which are subject to weaker interannual variability. The spectra at some tidal harmonics are overestimated presumably because, in general, the model is not dissipative enough and because tidal forcing in the llc4320 simulation was reported to be stronger than observed (Zhao et al., 2019). The comparisons of velocity spectra at 50 m and 200 m imply that the llc4320 simulation can reproduce realistic internal tides in the SCS.
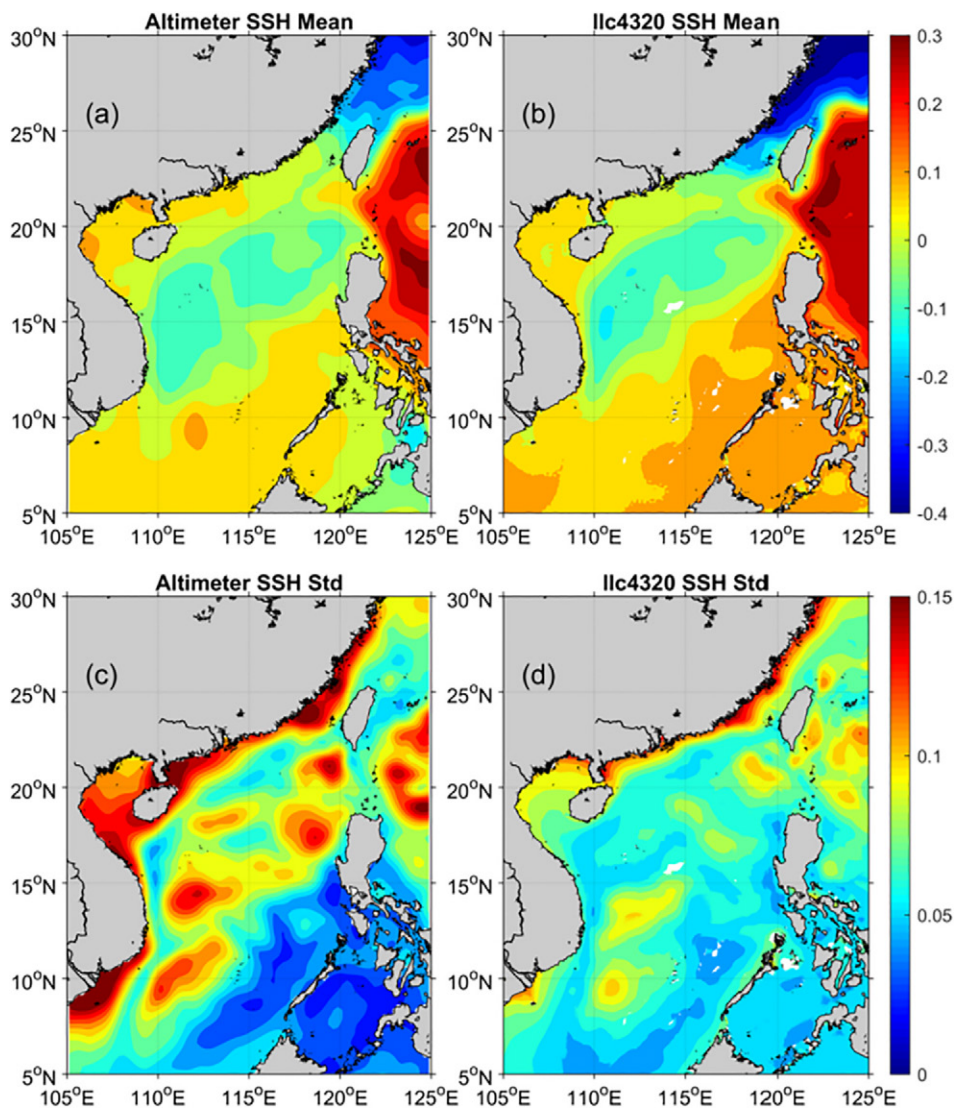
Fig. 2. Comparison of the (upper) mean and (lower) standard deviation of (left) observed and (right) simulated sea level (in m) in the SCS. All the calculations are based on 14-month-long data for both satellite and simulated SSH.

3.4. Tidal features

To evaluate the performance of the llc4320 simulation for tides, we generate the co-tidal charts of the major tidal constituents M_2, S_2, K_1 and O_1 based on the raw simulated sea level (Fig. 5). The amplitude of semidiurnal tides in the SCS deep basin is generally smaller (< 0.3 m) than that in the Pacific. In particular for the M_2 tide, the largest amplitude is found in the Taiwan Strait (> 2 m) and the East China Sea, and relatively large amplitude (about 1 m) is also evident around the Leizhou Peninsula and Mekong River Estuary. The co-phase lines indicate that semidiurnal tides propagate gradually from the Luzon Strait to the SCS basin. The diurnal tides have larger amplitudes in the SCS basin (about 0.5 m) compared to the semidiurnal tides. Relatively large amplitudes exist in the Beibu Gulf and Mekong River Estuary (about 0.5–1 m). Moreover, the K_1 tide is almost in phase over the entire SCS basin. The enhanced K_1 tidal amplitude (i.e., the amplitude gets increased from the Pacific to the SCS) and in-phase feature is attributed to the Helmholtz resonance by Zu et al. (2008). We note that the above tidal characteristics of the four major tidal constituents agree well, both qualitatively (in terms of spatial patterns) and quantitatively (in terms of amplitudes and phases), with an assimilative regional model of Zu et al. (2008) that was configured specifically to simulate the tides in the

SCS (compare Fig. 5 with their Figs. 2–4). The only discernible difference is that the co-phase lines of semidiurnal tides in Fig. 5a-b are less smooth than those in Zu et al. (2008), probably due to the impact of the multi-scale, complicated ambient currents in the llc4320 simulation that were not present in the tidal model of Zu et al. (2008).

The above model-data comparisons demonstrate that the llc4320 simulation is able to reproduce multi-scale processes in the SCS fairly well, in terms of both spatial patterns and temporal variability. Next we will use this model output to examine the submesoscale characteristics of the SCS.

4. Submesoscale characteristics and their seasonality in the SCS

This section first briefly illustrates the large-scale circulation in the SCS and then characterizes the overall features of submesoscale turbulence and its seasonality, by showing fields of relative vorticity (ζ), strain rate and divergence, skewness of ζ, vertical velocities and horizontal wavenumber spectra.

4.1. Basin-scale circulation

As submesoscale activities are highly related to the ambient large-
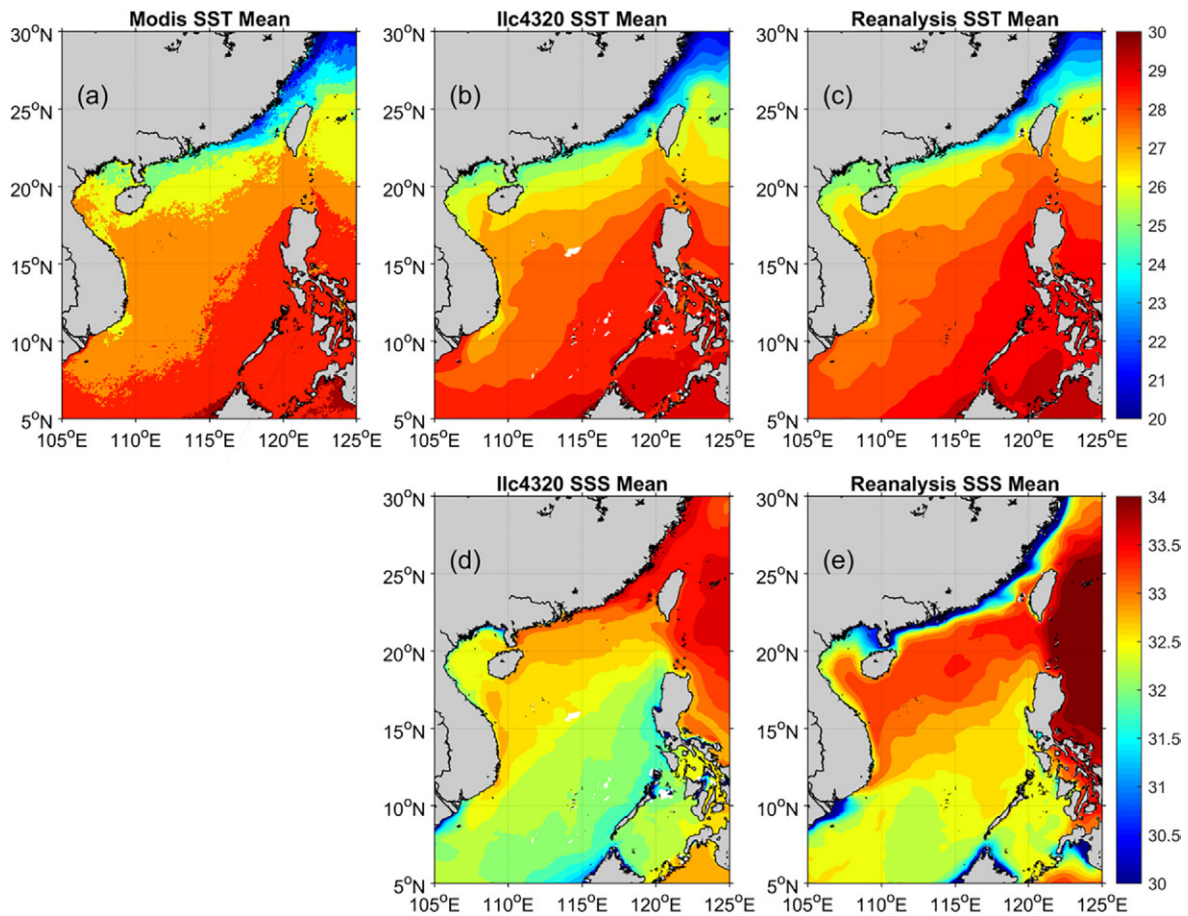
Fig. 3. Comparison of the mean sea surface (upper) temperature (in °C) and (lower) salinity calculated from (left) satellite data, (middle) llc4320 simulation and (right) CMEMS reanalysis.

scale and mesoscale circulations, it is useful to examine the basin-scale circulations in the SCS prior to investigating its submesoscale turbulence. Since the analysis of submesoscale features will be based on the llc4320 simulation, we also use this simulation to generate the mean SCS surface circulation in winter and summer. Here winter corresponds to (2011)December-(2012)January-February (DJF) and summer corresponds to (2012)June-July-August (JJA). The mean wintertime surface currents in the SCS are characterized by a cyclonic circulation with enhanced Kuroshio intrusion, relatively intense southward western boundary currents (WBCs), whereas the summertime currents feature a weaker anticyclonic circulation with a leaped Kuroshio path across the Luzon Strait and a northeastward jet off the southeastern Vietnamese coast (Fig. 6). The patterns of the mean SCS surface currents as well as their seasonality are in good agreement with previous studies based on observations or regional numerical simulations (e.g., Hu et al., 2000; Gan et al., 2006; Zu et al., 2019). The prominent seasonal variations in the basin-scale upper-ocean circulation of the SCS are driven primarily by the seasonally varying monsoons with northeasterly winds prevailing in winter and southwesterly winds in summer (Fang et al., 1998).

4.2. Snapshots and temporal variations

Following previous studies, we calculate three quantities to visualize the submesoscale features in the SCS. These include the vertical relative vorticity defined as $\zeta = v_x - u_y$, the strain rate defined as $strain = \sqrt{(u_x - v_y)^2 + (u_y + v_x)^2}$, and the divergence defined as $div = u_x + v_y$, where u and v are, respectively, zonal and meridional velocities, and the subscripts denote the corresponding derivatives.

Submesoscale processes are characterized by enhanced, localized ζ manifested as frontal/filamentous structures. These localized regions, with enhanced along-front velocities, are also accompanied by high *strain*, which includes both along-front stretching and cross-front shear (Mahadevan and Tandon, 2006; Mahadevan, 2019). High *strain* is also believed to induce frontogenesis and large vertical velocities (Mahadevan and Tandon, 2006; Verma et al., 2019). Therefore, ζ mainly depicts the balanced, rotational motions and *div* mainly reflects the unbalanced, wave motions, while both are mixed in the *strain* field.

Given the prominent seasonal changes in the SCS upper-ocean circulation, the local submesoscale turbulence may also have a strong seasonality. Fig. 5 shows the hourly snapshots of surface ζ, strain rate and divergence on January 1 and July 1, 2012. All fields have been normalized by the local planetary vorticity (f). Large values of normalized ζ, or equivalently the Rossby number ($Ro = \zeta/f$), can be easily found in both wintertime and summertime snapshots (Fig. 7a, d), suggesting that the SCS is swarming with submesoscale structures in both seasons. At the same time, robust seasonal differences could also be discerned in these fields. In winter, the ζ field indicates vigorous submesoscale activities in the northern SCS, along the western boundary of the SCS basin, and in the wakes of many islands experiencing intense flows (Fig. 7a). In summer, the northern SCS is slightly quiescent in terms of submesoscale processes compared to winter. By contrast, the area southeast of Vietnam has more energetic submesoscale vortices and filaments in summer (Fig. 7d), which is likely associated with the strong jet located in this region in a typical summer (Shaw and Chao, 1994). Comparing Figs. 6 and 7, it is clear that relatively intense large-scale flows are often accompanied by vigorous submesoscale activities, suggesting that the generation of submesoscale
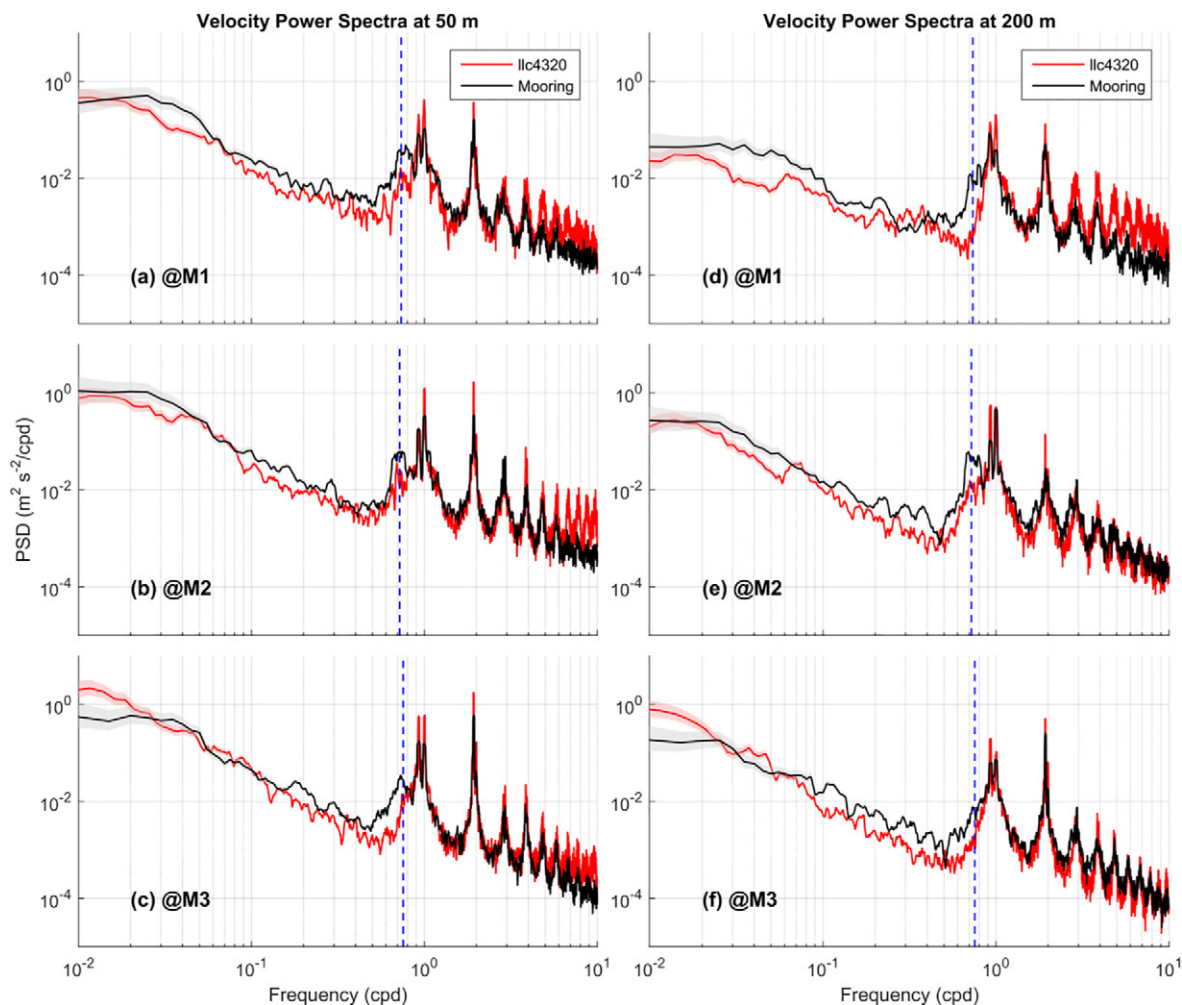
Fig. 4. Comparison of velocity power spectra at (left) 50 m and (right) 200 m estimated from the llc4320 simulation (red) and mooring measurements (black) at three mooring locations (M1, M2 and M3; Fig. 1). The blue dashed lines show the local inertial frequency. The shadings with lighter colors denote the 95% confidence intervals. (For interpretation of the references to color in this figure legend, the reader is referred to the web version of this article.)

processes is closely related to the ambient currents. Although submesoscale vortices are less visible in the strain field, we can also spot the submesoscale features at the western boundary in winter and off Vietnam in summer. Seasonal differences are also seen in the northern SCS, where internal-wave like patterns radiate southwestward into the deep basin in winter while they tend to propagate westward to the northern continental shelf in summer (Fig. 7b, e). Xu et al. (2016) identified two beams for the propagation of baroclinic energy flux of M_2 internal tide also based on numerical simulations, one propagating northwestward to the continental shelf and the other southwestward across the deep basin, but no seasonality was involved in their simulations. The divergence fields largely resemble the strain field in terms of the wave-like patterns, although submesoscale coherent structures are hardly seen at the western boundary and off Vietnam in the divergence fields (Fig. 7c, f).

In order to illustrate the temporal variability of submesoscale turbulence, we choose four areas according to the ζ fields (see black boxes in Fig. 7), and then examine the time variation of root mean square (RMS) of ζ. The RMS at each time step is calculated spatially for all ζ values in the selected area. The four areas include: i) the northern SCS (Region A) where the submesoscale turbulence experiences a clear seasonal cycle, ii) the western boundary of SCS (Region B) where an intense WBC strongly interacts with the Vietnamese coast in winter, iii) west of the Luzon Island (Region C) where submesoscale turbulence seems to be less active in both winter and summer, and iv) southeast of

Vietnam (Region D) where a strong jet separates from the Vietnamese coast and triggers vigorous submesoscale turbulence offshore by interacting with islands in summer. The seasonality is evident from the time series of ζ RMS in Region A with a peak in January (Fig. 8a). For Region B, the ζ RMS exhibits high values from October to December, during which time the SCS WBC is stronger (Fig. 8b). The average value of ζ RMS is the highest in Region B compared to other regions. In Region C, values of ζ RMS are relatively low and experience weak modulations throughout the year (Fig. 8c). In Region D, the time series of ζ RMS reveals two peaks around July and August, when the northeastward jet off Vietnam is strongest (Fig. 8d). Overall, the time variations of ζ RMS are all consistent with our expectation in the selected regions. It could therefore be viewed as indication of the intensity of submesoscale activities in the study area.

4.3. Skewness of the relative vorticity

Another perspective on characterizing the submesoscale turbulence is to examine the skewness of relative vorticity, ζ. As the third moment of a random variable, skewness measures the asymmetry of its probability density function. Negative skew refers to a longer or fatter tail on the left side of the distribution, while positive skew refers to a longer or fatter tail on the right. Large magnitudes of ζ skewness imply that there occasionally exist extraordinary large ζ magnitudes (compared to typical ζ values), manifested as long tails in the probability density
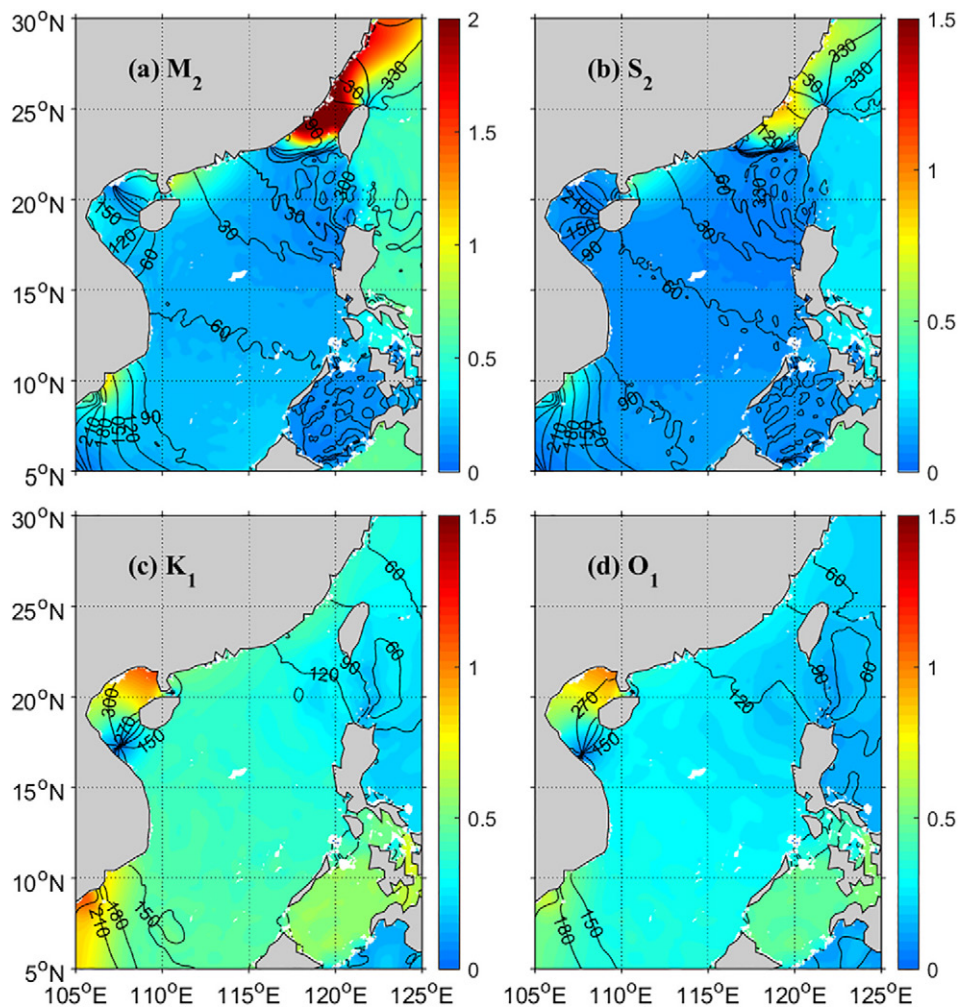
Fig. 5. Amplitude (color shading in m) and phase (contours in degrees) of co-tidal charts for tidal constituents (a) M_2, (b) S_2, (c) K_1 and (d) O_1 based on the raw sea level of llc4320 simulation.
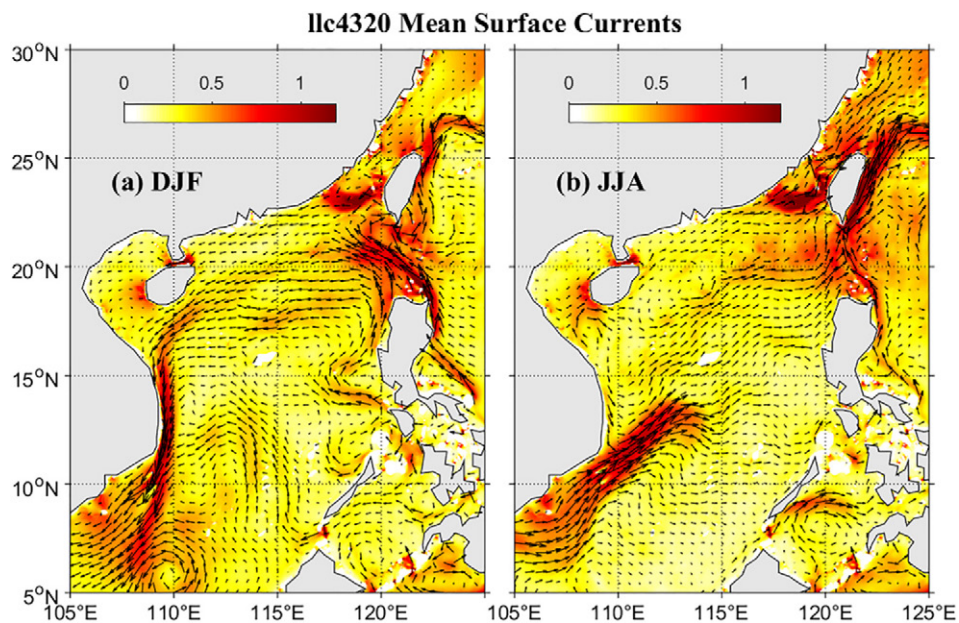
Fig. 6. Mean (a) wintertime (DJF) and (b) summertime (JJA) surface circulations in the SCS estimated from the llc4320 simulation. The color shading represents the average of velocity magnitude and vectors denote the averaged velocities.
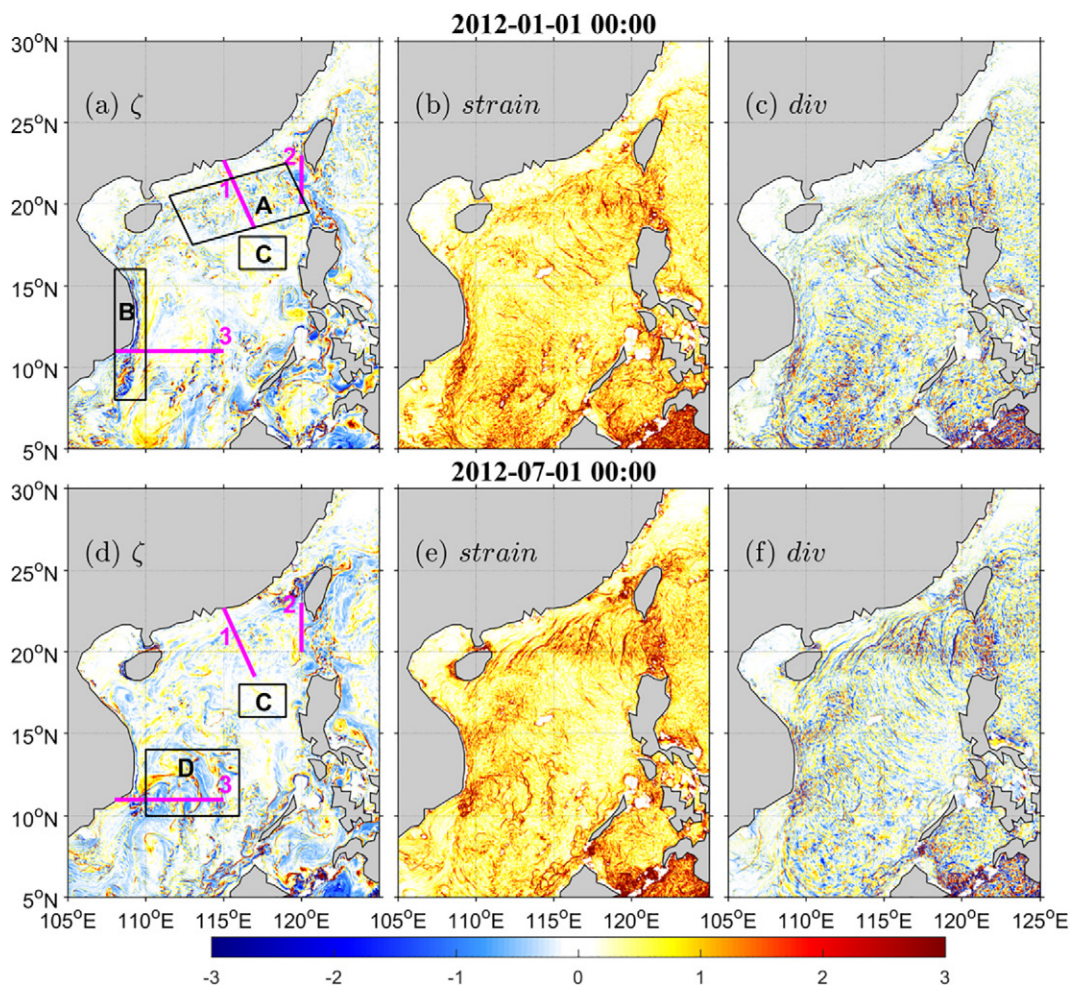
Fig. 7. Snapshots of surface (left) relative vorticity, (middle) strain rate and (right) divergence fields on (top) January 1 and (bottom) July 1, 2012 in the SCS based on the llc4320 simulation. All fields have been normalized by the local planetary vorticity. The thick magenta lines in the left panels are sections where vertical velocities will be examined in Fig. 10. The black boxes show the four selected regions where the RMS of ζ will be shown in Fig. 8. (For interpretation of the references to color in this figure legend, the reader is referred to the web version of this article.)
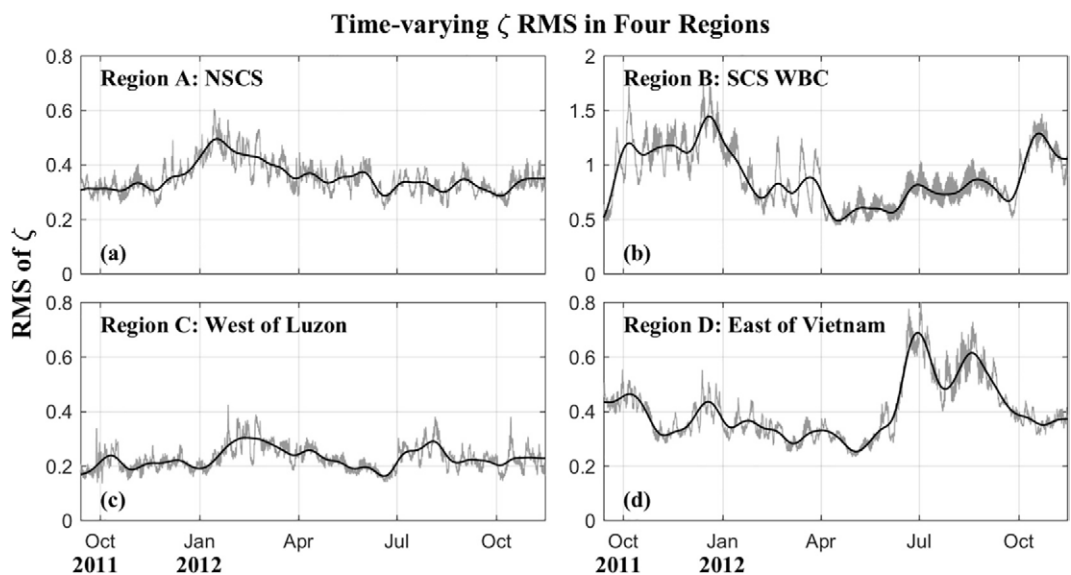
Fig. 8. Time series of spatial RMS of surface relative vorticity in the four selected regions shown in Fig. 7. Gray lines are the hourly time series and the thick black lines are their lowpass filtered version with a cutoff period of one month. Note that the y-axis of (b) has a different scale from the others.
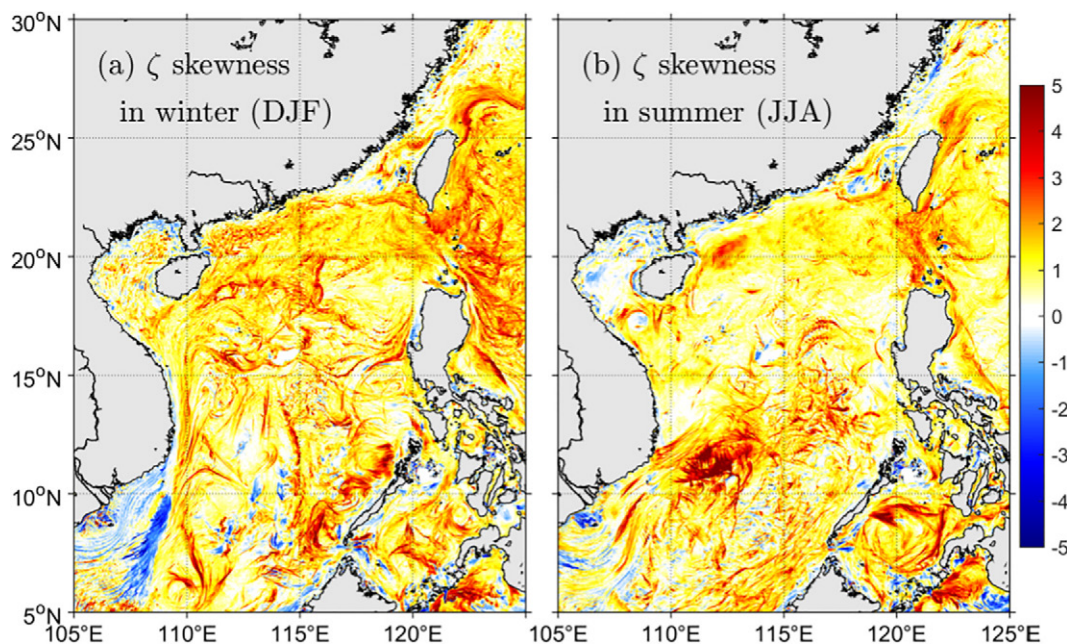
Fig. 9. Skewness of (a) wintertime and (b) summertime surface relative vorticity.

function of ζ distribution. This is often corresponding to sporadic intense submesoscale activities associated with large Rossby number.

We derive the spatial distributions of ζ skewness in winter and summer, each based on 3-month-long hourly time series of ζ at each grid point. The most conspicuous feature is the overwhelming positive ζ skewness in both seasons (Fig. 9), implying that the exceptionally large magnitude of vorticity in the upper ocean is primarily cyclonic. The positively skewed ζ distribution has previously been reported based on field observations and numerical simulations (e.g., Munk et al., 2000; Rudnick, 2001; Klein et al., 2008; Qiu et al., 2014; Buckingham et al., 2016). This asymmetry is normally explained by the fact that submesoscale instabilities tend to suppress the growth of anomalously strong anticyclones. This is related to Ertel's potential vorticity defined as,

$$q = (f\mathbf{k} + \nabla \times \mathbf{u})\cdot\nabla b \tag{1}$$

$$= (w_y - v_z)b_x + (u_z - w_x)b_y + (f + \zeta)N^2. \tag{2}$$

where b is buoyancy, N^2 is squared buoyancy frequency, and subscripts denote the derivatives. Different types of instabilities arise when $q < 0$ in the northern hemisphere. This could result from the strong baroclinicity that leads the first two terms of (2) to be negative which is termed as symmetric instability, or from strong anticyclonic vorticity that leads the last term of (2) to be negative which is termed as centrifugal instability (with $N^2 > 0$), or from prominent overturning with $N^2 < 0$ and termed as gravitational instability (Thomas et al., 2013). Hence centrifugal instability prevents the continuous growing of extreme negative ζ, whereas the growing of positive ζ would not be affected, which explains the dominance of large cyclonic vorticity. Nonetheless, we do identify patches of large negative ζ skewness in Fig. 9, which are generally seen in coastal regions or island wakes. This is because the topographic drag could possibly generate large negative ζ when the flow interacts with lateral boundary on its anticyclonic side (Gula et al., 2016).

Other mechanisms have also been proposed to interpret the predominance of cyclonic vorticity over anticyclonic vorticity in the upper ocean. For example, Mahadevan and Tandon (2006) used the semi-geostrophic dynamics to explain the dominance of cyclonic vorticity. They also proposed that the relation between vorticity and Richardson number derived by Pedlosky (1987) (cf. Equation 8.4.67) could be used

as an explanation. In a study of wind-forced near-inertial motions in a geostrophic current, Whitt and Thomas (2015) found that anticyclonic geostrophic flow is more vulnerable to be dampened than the cyclonic counterpart in high Rossby number regimes, which explains the positively skewed ζ distribution in the upper ocean.

4.4. Vertical velocities

Submesoscale turbulence is often accompanied by much larger vertical velocities (W), particularly in the upper ocean, compared to those induced by mesoscale processes (e.g., Thomas et al., 2008; McWilliams, 2016). Based on simulations without tidal forcing, previous studies indicated that W in regions with vigorous submesoscale turbulence reaches ~ 100 m d^{-1} (~10^{-3} m s^{-1}) in the SCS (Dong and Zhong, 2018), similar to the W values in the open ocean (e.g., Capet et al., 2008a). Under strong influence of tides, however, we expected magnitudes of W to be rather different. Three transects are selected to investigate this issue (thick magenta lines in Fig. 7): i) transect 1 is a cross-shelf section that is roughly perpendicular to the 200-m and 1000-m isobaths in the northern SCS where active submesoscale turbulence is present in winter; ii) transect 2 is a meridional transect (120°E) to the northwest of the Luzon Strait that transverses an anticyclonic eddy associated with the Kuroshio Loop; and iii) transect 3 is a zonal transect (11°N) to the southeast of Vietnam where submesoscale processes are active in summer.

The raw W values in all the three transects reach 0.01 m s^{-1} (~1000 m d^{-1}) or even higher (Fig. 10), which are one order of magnitude larger than previously reported W values in the SCS based on non-tidal simulations. We thus try to isolate super-inertial motions (including tides and internal waves of various frequencies) from the balanced motions by simply applying a temporal filter with a cutoff period of 3 days to the W time series at each grid point. The highpass filtered W (presumably dominated by tides and internal waves of various frequencies) is almost identical to Fig. 10 (not shown) and the lowpass filtered W values (presumably dominated by balanced motions) are generally weaker than their raw values by an order of magnitude (Fig. 11). This demonstrates that the vertical motions in the SCS are dominated by tides and internal waves.

The typical magnitude of raw W is the largest in transect 2, followed by transect 1 and then transect 3 (Fig. 10). This is expected since the
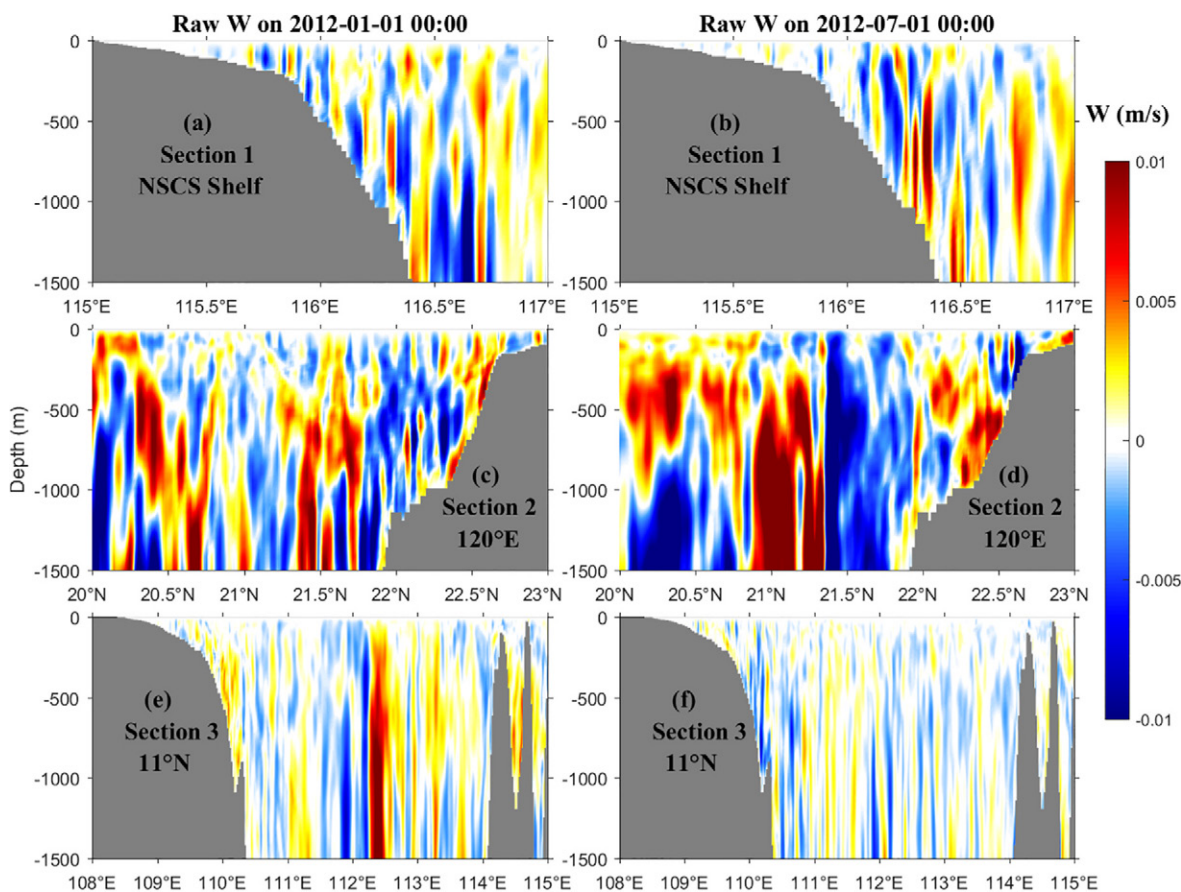
Fig. 10. Distributions of raw vertical velocities (W, in m s^{-1}) along the (top) cross-shelf transect in the northern SCS (transect 1), (middle) meridional transect along 120°E (transect 2) and (bottom) zonal transect along 11°N (transect 3), on (left) January 1 and (right) July 1, 2012. The three sections are shown as thick black lines in Fig. 7.

internal tides are the strongest in the vicinity of the Luzon Strait, which is regarded as one of the most important generation sites for internal tides (Alford et al., 2015). The internal tides then propagate westward to the northern SCS shelf and southwestward to the deep basin. Increasing distance from the source region is accompanied by decreasing magnitude of W. This is independent of time variation. Overwhelmed by tidal motions, the signature of anticyclonic eddy is not clear in Fig. 10c. When tides and internal waves are removed, we do identify enhanced vertical velocities (albeit secondary compared to the high-frequency W) in the upper mixed layer associated with active submesoscale processes, for example, the northern SCS shelf in winter (Fig. 11a) and the offshore area of transect 3 in summer (Fig. 11f). Nonetheless, the magnitude of lowpass filtered W follows the same sequence of the raw version, i.e., largest in Luzon Strait and weakest to the southeast of Vietnam. We speculate this is related to the local mesoscale processes but more conclusive evidence is required. Enhanced lowpass filtered W is also found at continental slopes, where submesoscales are also expected to be active due to topographic drag-induced instabilities. The wintertime continental slope off Vietnam is a good example due to the strong interactions of topography and intense WBCs (Fig. 11e).

The horizontal distributions of W are also mapped in order to view the general pattern and magnitudes of W at different depths (Fig. 12). The internal-wave signals are evident in snapshots of W, although the magnitude of W gets intensified and the pattern gets more complex with increasing depth. The RMS of surface W is typically smaller than the order of 10^{-4} m s^{-1} in the SCS basin but is much larger at nearshore regions due to barotropic tides, in particular from the shelf of the East China Sea to the Taiwan Strait. Interestingly, the magnitude

distribution of surface W is rather similar to the M$_2$ cotidal chart (Fig. 5a). An important implication from this similarity is that in addition to the often-examined horizontal velocity fields (e.g., Lahaye et al., 2019), internal tides also have prominent imprints on the surface W field. Although the rigid-lid approximation is often assumed in theoretical investigations (e.g., D'Asaro, 1978; Lahaye et al., 2019) to simplify the analysis, the llc4320 simulation uses an implicit free surface formulation, which permits internal tides to have non-zero W at the sea surface. High RMS values of W at 5 m, of order $O(10^{-4})$ m s^{-1}, extend from Luzon Strait northwestward to the shelf of northern SCS. High RMS values of W at 200 m are also found in the vicinity of Luzon Strait, of order $O(10^{-3})$ m s^{-1} or even higher, and spread southwestward to the SCS basin. By drastic contrast, the coherent internal wave signals are removed in the 3-day lowpass-filtered W snapshots (Fig. 13). Instead, they reveal abundant submesoscale features and the pattern bears some resemblance to the snapshots of surface ζ (compare Fig. 7a, d and 13), implying that vigorous submesoscale processes are accompanied by enhanced lowpass filtered W, as one would expect.

We could conclude from the above results that vertical velocities in the upper mixed layer of the SCS are dominated by tidal motions, particularly in the vicinity of Luzon Strait. If the tides are removed, large vertical velocities are found in areas with enhanced submesoscale activities. Below the mixed layer, the raw vertical velocities are dominated by internal waves (particularly internal tides), while the lowpass filtered ones are controlled primarily by mesoscale processes. Here we have removed these super-inertial wave motions by applying a temporal lowpass filter with a cutoff period of 3 days. We recognize that the 3-day lowpass filter is not the best approach to separate tidal and submesoscale motions, and the lowpass filtering might have also
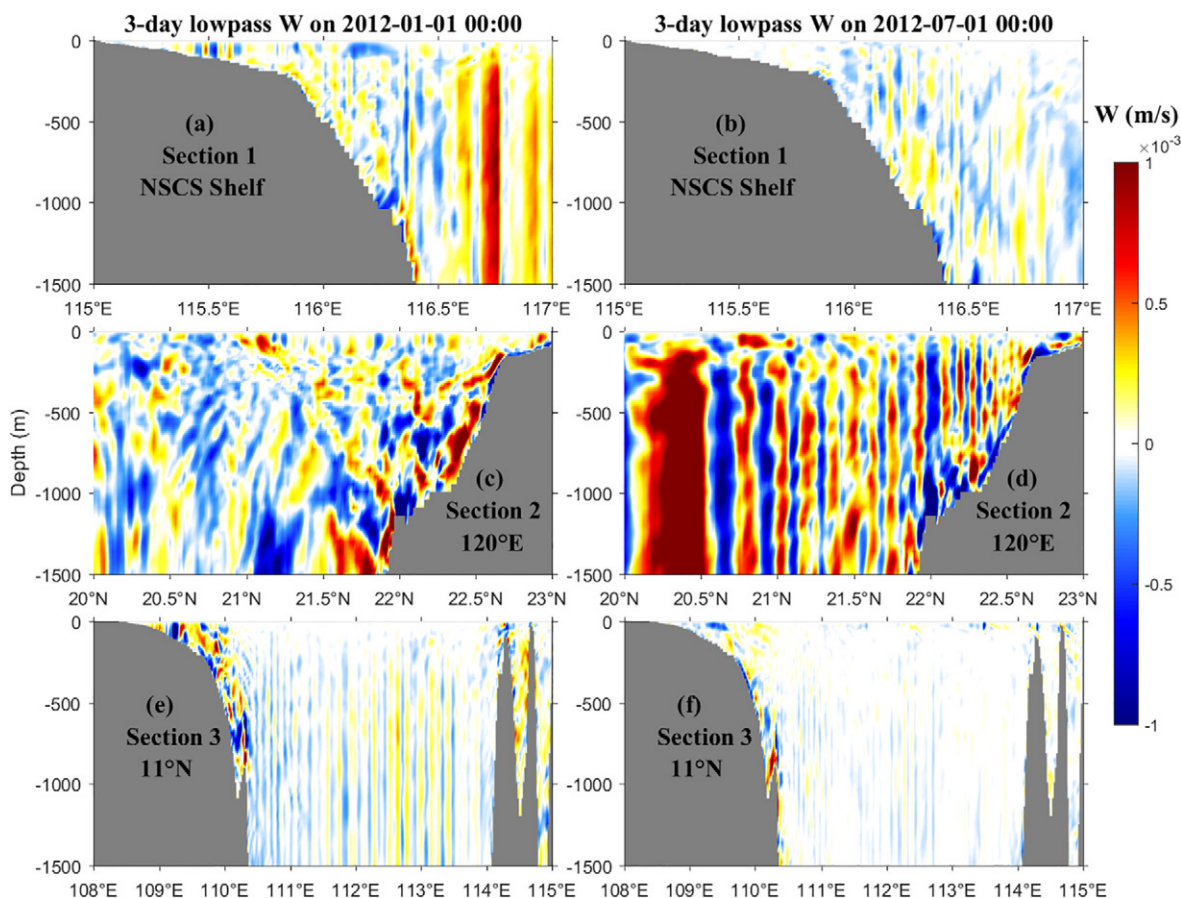
Fig. 11. Same as Fig. 10 but for the 3-day lowpass filtered *W*.

removed some submesoscale signals that have a timescale near the cutoff period. Nevertheless, the spatial patterns of lowpass-filtered *W* and the surface ζ do bear some resemblance, implying that lowpass filters with appropriate cutoff periods could be useful in separating the super-inertial unbalanced wave motions and the lower-frequency balanced motions in the SCS. There are more sophisticated techniques for such decomposition. For instance, recent studies have proposed methods using the frequency-wavenumber spectra (e.g., Lahaye, et al., 2019; Torres et al., 2019), but their applications to regional analysis are challenging provided the two-dimensional time–space Fourier transform nature.

4.5. Wavenumber spectra

We first compare the horizontal wavenumber spectra of sea level from the llc4320 simulation and along-track altimeter, respectively, at the satellite tracks of Cryosat-2. The comparison is conducted separately on the northern SCS shelf and in the SCS basin, and also separately in winter (DJF) and summer (JJA). Each transect has a length of ~ 400 km on the northern SCS shelf and of ~ 900 km in the SCS basin (figure not shown). The wavenumber spectra are calculated from the fast Fourier transforms (fft) of along-track sea level and subsequently averaged over all transects in each season. The spectral scaling of observed sea level spectra is closer to k^{-3} at scales larger than 100 km and flatter (shallower than k^{-2}) at scales shorter than 100 km (Fig. 14). This holds for both wintertime and summertime observed spectra on the shelf and in the basin. The simulated spectra, however, fall closer to the k^{-2} scaling at both locations and in both seasons. The along-track altimeter data obtained from the CMEMS also include the tidal components of sea level, but the tides are aliased due to gaps in satellite tracks and the relatively long repeat period. Although these

errors have been considered in producing the tidal components, some errors nevertheless remain caused by non-stationary or incoherent internal tides. If the tidal components are included, the observed sea level spectral magnitudes are slightly higher than the non-tidal counterparts on the shelf but the power law remains similar (Fig. 14a-b). The tidal and non-tidal observed sea level spectra are almost identical in the SCS basin (Fig. 14c-d), because tidal signals are rather weak in the basin. The energy level of simulated sea level, embedded with hourly tidal forcing, is apparently higher than the observed spectra roughly by an order of magnitude.

The horizontal wavenumber spectra of kinetic energy (KE) based on the llc4320 simulation are then estimated at the satellite tracks. It is shown that the KE level is constantly higher in winter than in summer on the northern SCS shelf (Fig. 15a). The opposite occurs in the SCS basin, i.e., the KE level is higher in summer (Fig. 15b). The higher KE on the shelf in winter is likely associated with enhanced submesoscale activities in this region. As shown in Fig. 7, the northern SCS shelf is rich in internal waves during summer. Both phenomena in the two seasons tend to render the KE wavenumber spectra to have a k^{-2} scaling, consistent with the spectral slopes over the range between 10 and 100 km (Fig. 15a). The higher KE in the basin during summer is possibly due to the elevated submesoscale filaments/vortices to the east of Vietnam associated with jet-island interactions (Fig. 7d). Again, the spectral scaling falls close to k^{-2} over the range between 10 and 100 km (Fig. 15b). For scales larger than 100 km, the summertime KE wavenumber spectrum in the SCS basin has a spectral slope close to k^{-3}, while the wintertime spectrum in the basin and the spectra on the northern SCS shelf all have a spectral slope shallower than k^{-2}.
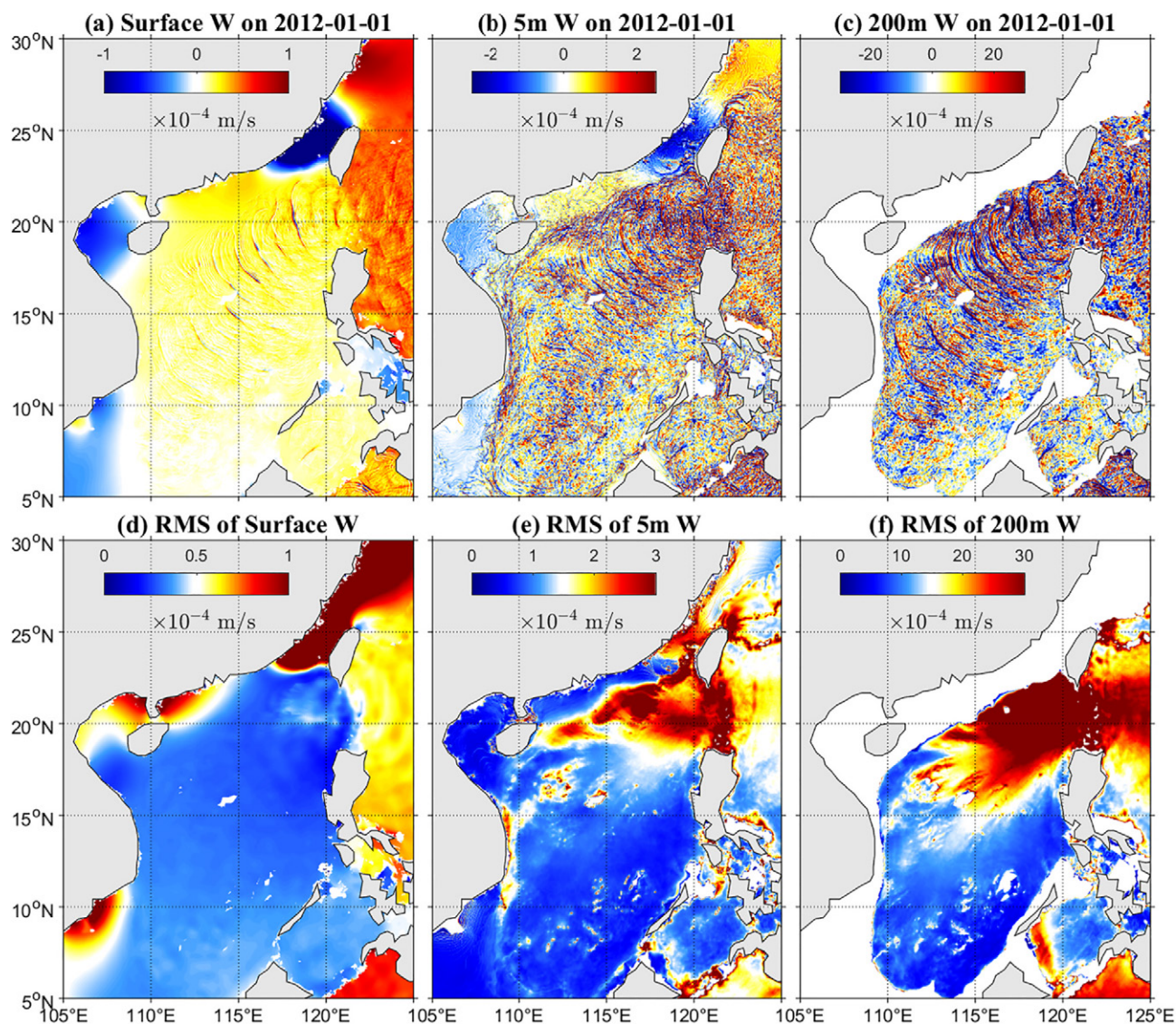
Fig. 12. Spatial (top) snapshots of the raw vertical velocities (*W*) on January 1, 2012 and (bottom) RMS of *W* for (left) surface, (middle) 5 m and (right) 200 m.

5. Key regions

Several key regions of the SCS can be identified in terms of the activeness of submesoscale processes. Below, we try to inspect these regions more closely by examining the surface fields of more variables.

5.1. Northern SCS

Surface fields of ζ, sea level (η), density gradient magnitude ($|\nabla\rho|$), vertical velocity (*W*), strain rate and divergence in the northern SCS and Luzon Strait are shown in Fig. 16 for wintertime snapshot and in Fig. 17 for summertime snapshot. In the northern SCS, the ζ map reveals abundant submesoscale vortices and filaments in winter, whereas the ζ field is much smoother in summer. The robust seasonality of submesoscale turbulence in this region has been reported by previous investigators based on simulations without tidal forcing (Dong and Zhong, 2018) and is explained by the seasonal differences in the flow straining (via frontogenesis) and mixed-layer depth (via mixed-layer instability). In fact, the wintertime and summertime snapshots share a feature that the distributions of ζ and $|\nabla\rho|$ align closely with each other, implying that the frontogenesis is also important in forming the summertime submesoscale turbulence in this region. High resemblance between the distributions of strain rate and divergence is found in both

seasons but it is interesting to note that the distribution of strain rate also bears some similarity to the map of $|\nabla\rho|$ in winter, which is not seen in summer.

The llc4320 simulation is unique because it includes tidal forcing, illustrating features in maps of certain variables that are not seen in the previous non-tidal simulations. For example, the internal-tide signals are clearly discernable in snapshots of η, near-surface *W*, and divergence. After generation in the Luzon Strait, the internal waves propagate westward and northwestward to the northern SCS (e.g., Bai et al., 2014), illustrated in the fields of near-surface *W* and strain/divergence, respectively. In addition, there is also clear seasonality in the activities of internal waves on the continental shelf of the northern SCS. In winter, internal waves propagate westward from the Luzon Strait but are terminated at the continental slope, with rather small magnitudes of strain rate and divergence on the shelf (Fig. 16). In summer, however, the internal waves continue to propagate northwestward to the shelf (Fig. 17). This seasonal difference is presumably due to the seasonality in the stratification, i.e., the wintertime upper ocean is relatively mixed on the continental shelf compared to summer, unfavorable for the generation and propagation of internal waves.
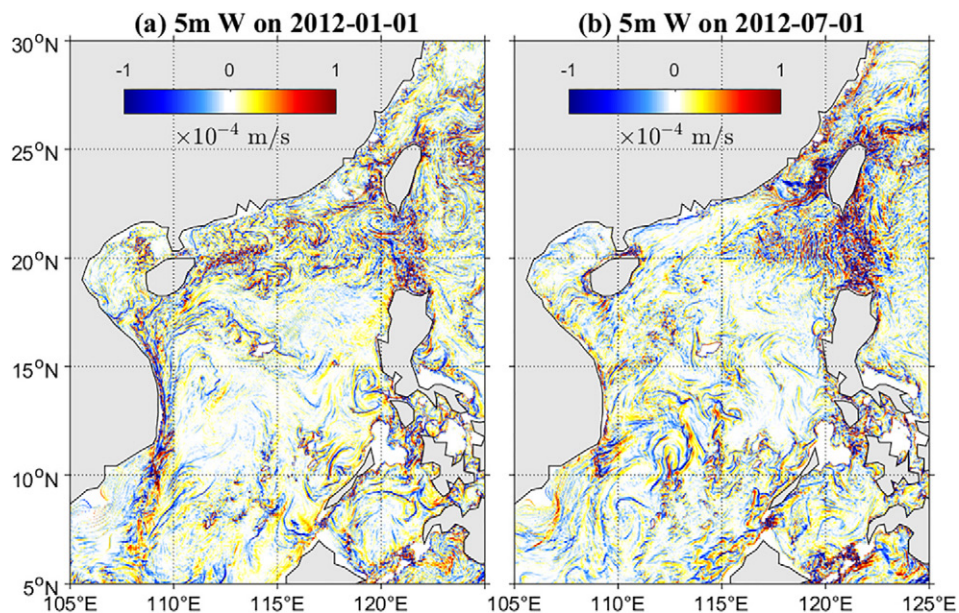
Fig. 13. Snapshots of 3-day lowpass filtered *W* at 5 m on (a) January 1 and (b) July 1, 2012.

5.2. Luzon Strait

Luzon Strait is one of the most important source regions for internal waves (e.g., Alford et al., 2015). Moreover, the Kuroshio often intrudes the SCS in winter with a large loop to the northwest of Luzon Strait. So, Luzon Strait is of particular interest in examining the local
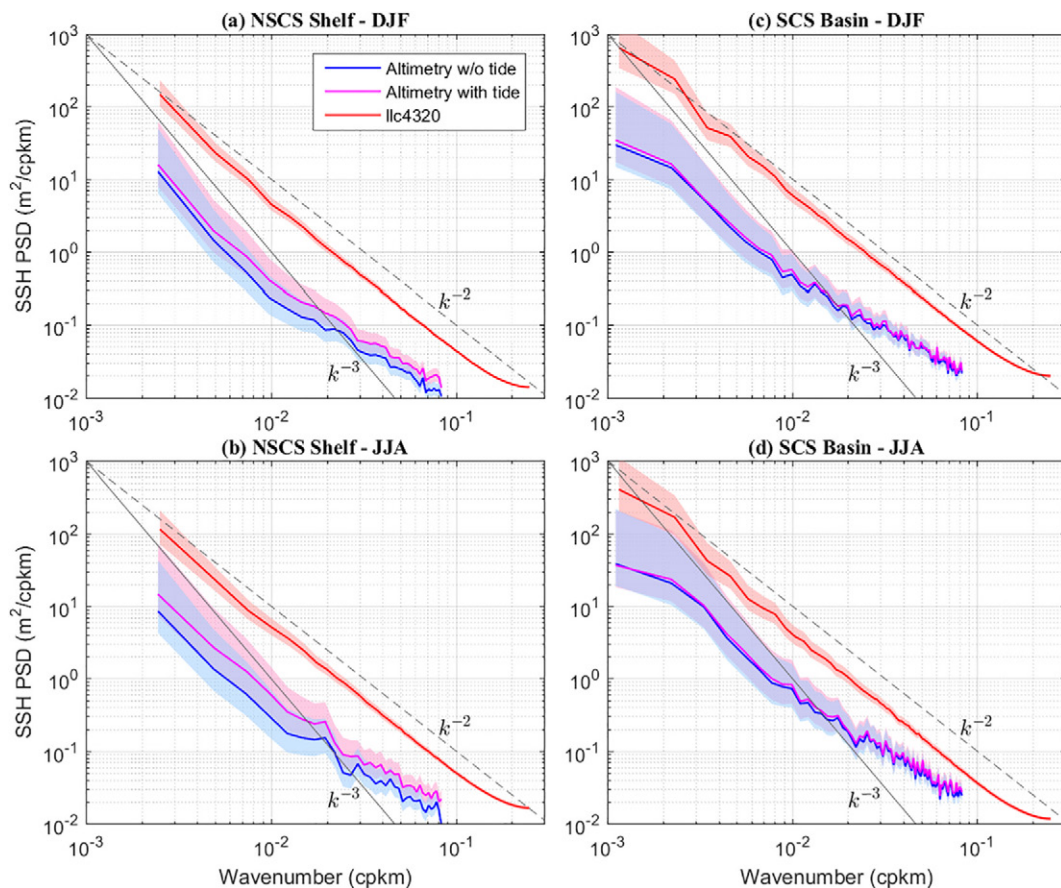
Fig. 14. Wavenumber spectra of sea level from along-track altimeter Cryosat-2 (blue and magenta curves) and the llc4320 simulation (red curves). The spectra are estimated separately (left) on the northern SCS shelf and (right) in the SCS basin in (upper) winter and (lower) summer. The blue curves represent the observed spectra based on sea level without tidal components whereas the magenta curves are for those including tides. The corresponding shadings with lighter colors represent the 95% confidence intervals of the spectral estimates. (For interpretation of the references to color in this figure legend, the reader is referred to the web version of this article.)
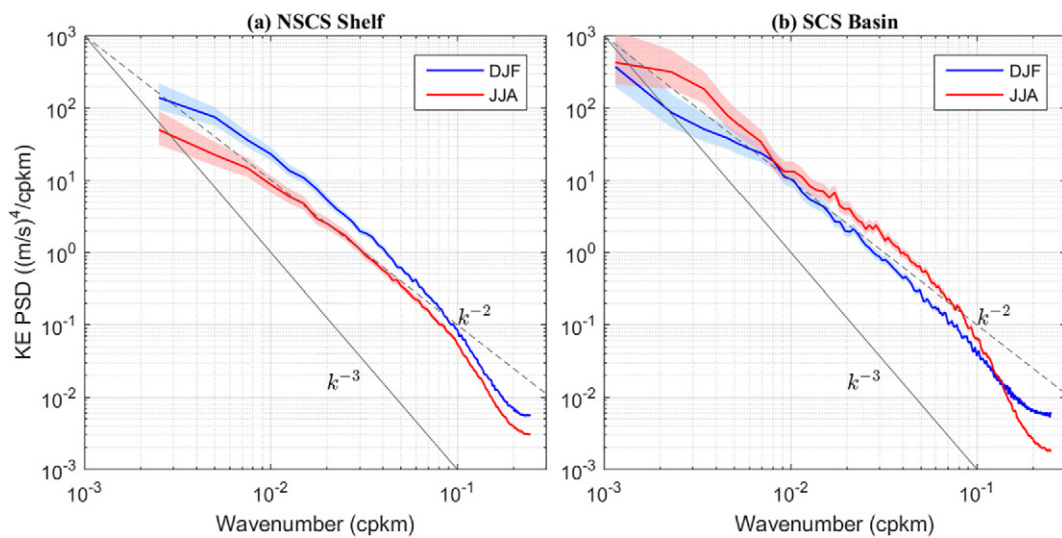
Fig. 15. Horizontal wavenumber spectra of surface kinetic energy calculated from the llc4320 simulations at the satellite tracks of Cryosat-2.
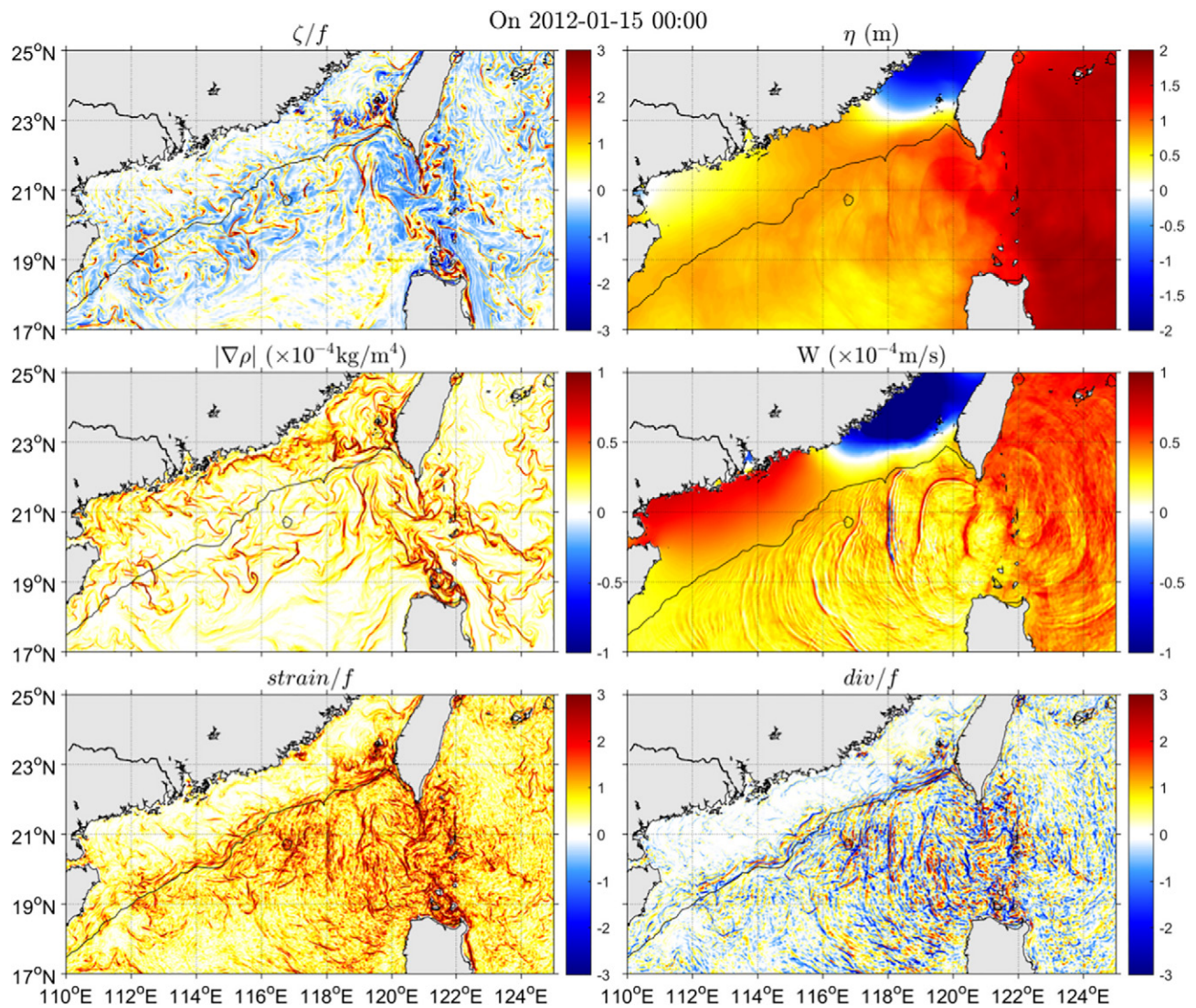
Fig. 16. Snapshots of surface ζ, sea level (η), density gradient magnitude ($|\nabla\rho|$), vertical velocity (W), strain rate and divergence on January 15, 2012 for northern SCS and Luzon Strait. The black line in each panel shows the 200-m isobath.
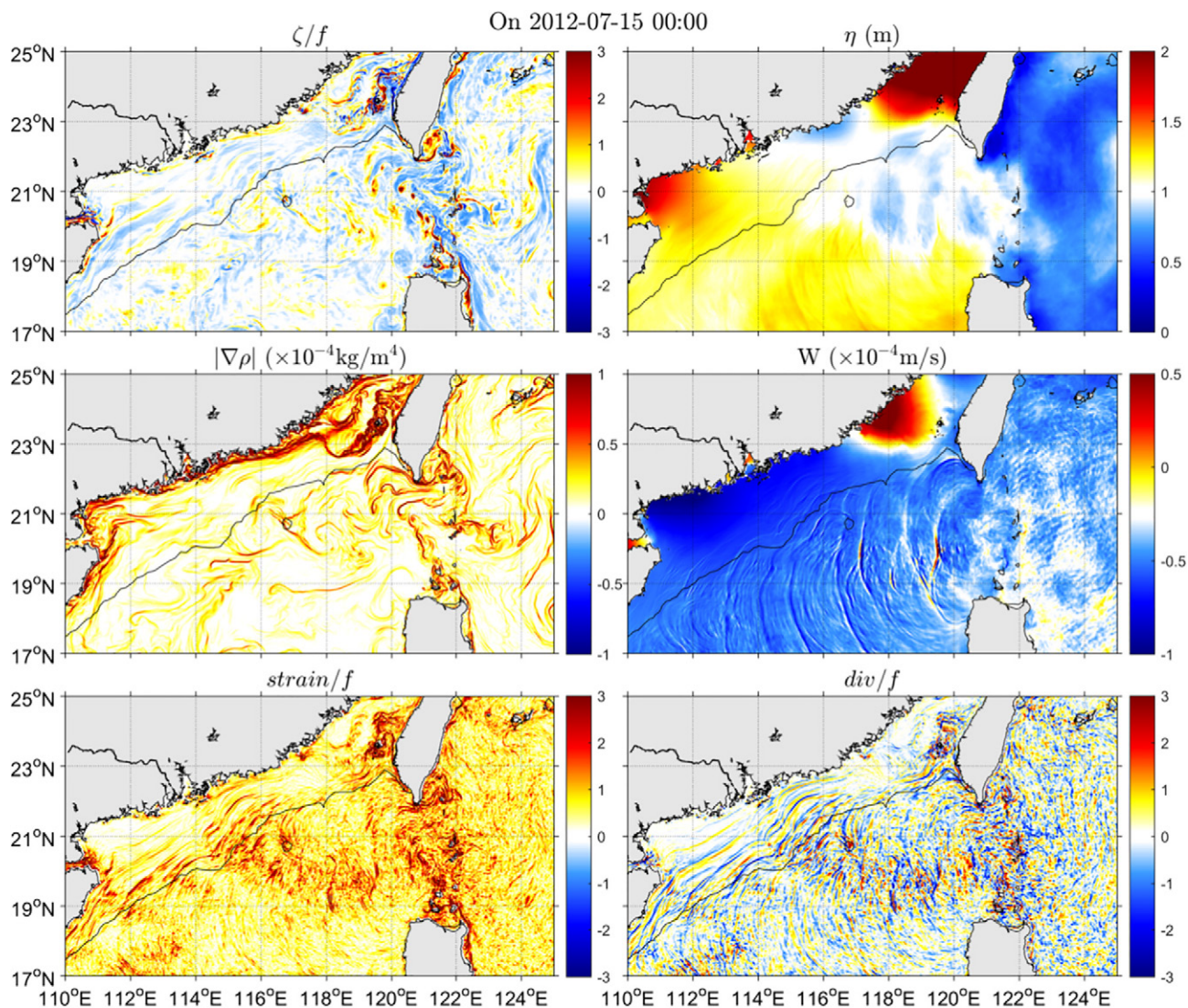
Fig. 17. Same as Fig. 16 but for July 15, 2012.

submesoscale characteristics. As shown in Fig. 16, the llc4320 simulation is generally able to reproduce the anticyclonic wintertime Kuroshio loop to the northwest of the strait. Filaments with relatively high positive ζ are observed along the periphery of the loop, which bounds an area with negative ζ. These filaments also coincide with areas where the magnitudes of $|\nabla\rho|$ are large.

During the intrusion into the SCS, the Kuroshio also interacts with islands in Luzon Strait, triggering filaments with large magnitudes of ζ in their wakes. When the Kuroshio path encounters islands at a right angle, trains of coherent submesoscale vortices are continuously generated in the wakes. This is particularly evident in the summertime snapshot of ζ (Fig. 17). The generation mechanism needs more in-depth investigations although previous studies provided possible explanations in terms of barotropic instability due to horizontal velocity shear (Gula et al., 2016). Maps of η, W, strain rate and divergence have similar large-scale patterns, which clearly show that internal waves are generated in the Luzon Strait and radiate both westward to the SCS and eastward to the western Pacific. The distribution of strain rate reflects signals of both strong fronts and internal waves, just like its wintertime counterpart in the northern SCS.

5.3. SCS western boundary current region in winter

The WBC of the SCS basin has been investigated for decades. The

reader is referred to Fang et al. (2012) for a review on studies of the SCS WBC. Unlike the WBCs in the open ocean, the SCS WBC is seasonally reversible and might also be related to the El Niño event (Zhao and Zhu, 2016). Compared to summer, the wintertime WBC is narrower and much stronger flowing southward along the coast of Vietnam. As mentioned in Section 4, the strong interactions between the WBC and the coast result in an elongated filament of large negative vorticity (Fig. 18), which could be favorable for the development of centrifugal instability. The WBC separates from the Vietnamese coast at about 11°N and continues to flow southward, getting slightly broader in width. The southward flowing current encounters some islands after separation, which triggers submesoscale vortices in wakes. Submesoscale structures in the offshore areas are mostly long filaments revealed in the distributions of ζ, $|\nabla\rho|$ and strain rate. The signal of internal waves, shown in the maps of η, W and divergence, is much weaker than that in the northern SCS since the southwestern SCS is pretty far away from the source region.

5.4. East of Vietnam in summer

In summer, the upper SCS is structured as a double-gyre circulation with a northeastward jet in between (e.g., Shaw and Chao, 1994), which is seen in the maps of ζ, $|\nabla\rho|$, strain and η (Fig. 19). The jet is in fact also viewed as part of the SCS WBC in summer (Fang et al., 2012).
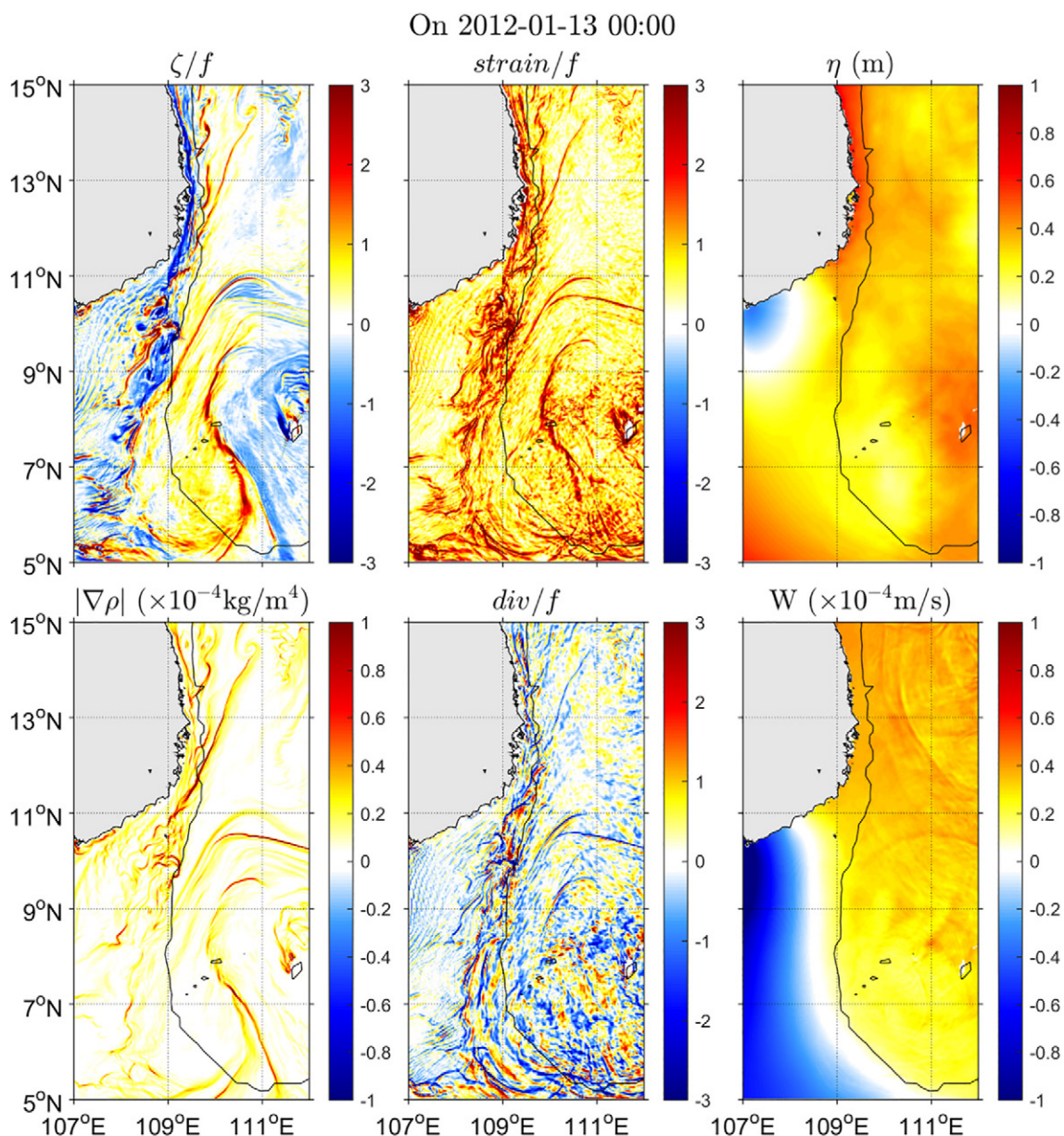
Fig. 18. Snapshots of surface ζ, density gradient magnitude ($|\nabla\rho|$), strain rate, divergence, sea level (η) and vertical velocity (W) along the western boundary of the SCS on January 13, 2012. The black line in each panel shows the 200-m isobath.

The most striking submesoscale feature associated with this jet is the trains of submesoscale vortices with alternating signs of vorticity, which are formed by the jet-island interactions in their wakes and advected to the east of Vietnam. Similar submesoscale vortex trains in this region have also been found by high-resolution satellite observations (e.g., Liu et al., 2015; Yu et al., 2018), and the generation mechanisms have arguably been attributed to frontal/shear instabilities. Immediately north of the vortex trains, an elongated filament with positive ζ also extends northeastward. Therefore, filaments and submesoscale vortices together constitute the main summertime submesoscale structures to the east of Vietnam, generated primarily by flow-topography interactions.

6. Summary and discussion

The mesoscale and submesoscale features in the SCS are characterized in this study based on a submesoscale-permitting numerical simulation (MITgcm llc4320) with nominal horizontal grid spacing of

1/48°, approximately 2.2 km in both zonal and meridional directions in the SCS region. Compared to previous studies, one unique feature of this simulation is the explicit inclusion of tidal forcing in this tidally energetic marginal sea. The model output is first evaluated against satellite observations, reanalysis data, and *in situ* mooring measurements. It is shown that the MITgcm llc4320 simulation is generally capable of reproducing a wide spectrum of dynamical processes in the SCS, including basin-scale circulation, internal tides, and mesoscale/submesoscale variabilities.

The model output is then used to illustrate the particular submesoscale characteristics of the SCS, and a few key findings are outlined below. (i) The results reveal abundant submesoscale features (e.g., vortices, filaments) both in winter and summer. Strong seasonality in terms of the activeness of submesoscale turbulence exists in many regions, for example the northern SCS, the SCS WBC region, east of Vietnam, etc., which could be due to the difference in mixed-layer depths and flow straining. (ii) The distribution of relative vorticity (ζ) generally shows positive skewness, particularly in the offshore regions.

On 2012-08-13 00:00
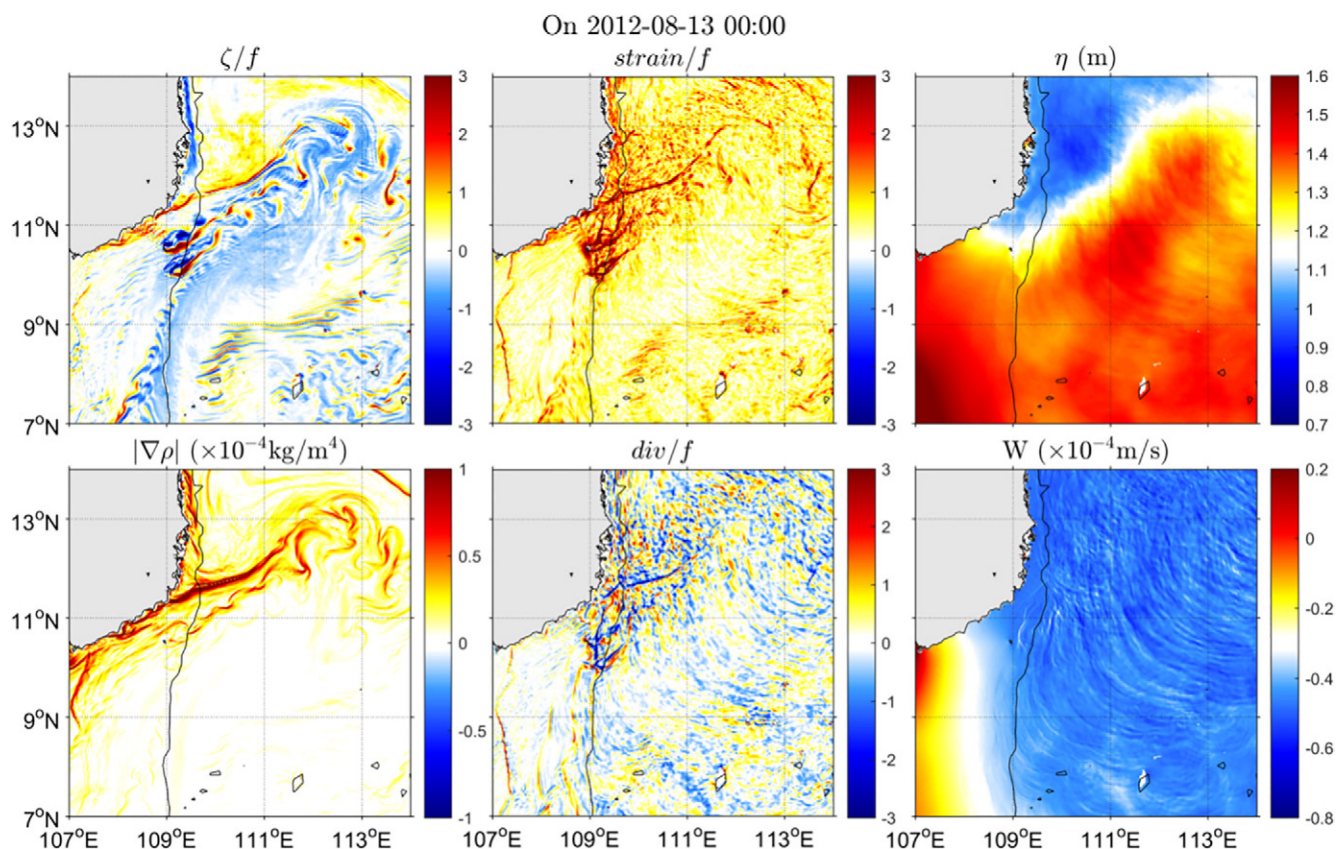
Fig. 19. Same as Fig. 18 but for the east of Vietnam on August 13, 2012.

This is expected to be caused by the suppression of large anticyclonic vorticity due to centrifugal instability. However, patches of large negative ζ are still seen in, for example, the SCS western boundary in winter, island wakes, etc. (iii) Strong vertical velocities in the llc4320 simulation, which includes tidal forcing, can reach as much as 0.01 m s^{-1}, about an order of magnitude larger than those in simulations without tidal forcing. In fact, the vertical motions in the upper SCS are overwhelmed by tidal modulations instead of the often-asserted submesoscale processes. (iv) Both the wintertime and summertime horizontal wavenumber spectra of kinetic energy have a spectral scaling close to k^{-2} over the range between 10 and 100 km. This occurs both on the northern SCS shelf and in the SCS basin. Both the enhanced submesoscale activities and internal waves tend to render the horizontal wavenumber spectra of kinetic energy to have a k^{-2} scaling.

Submesoscale features in a few key regions of the SCS are also examined in more detail. (i) The northern SCS experiences robust seasonality in terms of submesoscale turbulence with enhanced submesoscale vortices/filaments in winter while smoother, wave-like patterns in summer. Internal waves on the continental shelf of the northern SCS also have clear seasonality, which is likely related to changes in the local stratification. (ii) The Luzon Strait is source to energetic internal waves in the surrounding area. It is also rich in many mesoscale-driven submesoscale structures due to Kuroshio intrusions and mesoscale eddies in the vicinity of the strait. The strong Kuroshio-island interactions also trigger trains of submesoscale vortices and filaments under certain circumstances. (iii) The SCS WBC in winter features a narrow and intense southward flow along the coast of Vietnam. The flow strongly interacts with the coast on its anticyclonic side, resulting in filaments with large negative ζ, which could be favorable for development of submesoscale instabilities. (iv) During summer, a northeastward jet separates from the Vietnamese coast and triggers submesoscale vortex streets due to jet-island interactions, which have been verified by high-resolution satellite observations.

Although the MITgcm llc4320 simulation is generally capable of reproducing many dynamical processes in the SCS both spatially and temporally, there is room for improvement. For example, the river runoff imposed in the model is time-mean and diffuse, which leads to inaccurate patterns of the China Coast Current during winter, in particular in the salinity structure. Better representation of river runoff would result in more realistic coastal currents and hence more realistic frontal structures in the East China Sea and the Taiwan Strait. This would help reproduce the submesoscale dynamics/instabilities at the fronts in this region. Another area for further studies based on this model simulation is the realization of regional, higher-resolution simulations (via regional nesting) that could better resolve, for example, the flow-topography interactions. Filaments or small vortices induced by the submesoscale instabilities associated with such interactions generally require the model grid spacing to be finer than 1 km. Ultimately, the dedicated design of high-resolution observations is beneficial in advancing our understanding of submesoscale dynamics and also in improving the model performance. This is an ongoing effort of the community and a variety of observational techniques have been developed over the past few years, for example, towed measurements in frontal regions as well as synergistic networking with multiple instruments targeted on a specific phenomenon.

Declaration of Competing Interest

The authors declare that they have no known competing financial interests or personal relationships that could have appeared to influence the work reported in this paper.

Acknowledgments

References

Alford, M.H., Peacock, T., MacKinnon, J.A., et al., 2015. The formation and fate of internal waves in the South China Sea. Nature. 521 (7550), 65–69.

Bai, X., Liu, Z., Li, X., Hu, J., 2014. Generation sites of internal solitary waves in the southern Taiwan Strait revealed by MODIS true-colour image observations. Int. J. Remote Sens. 35 (11–12), 4086–4098.

Blumen, W., 1978. Uniform potential vorticity flow: Part I. Theory of wave interactions and two-dimensional turbulence. J. Atmos. Sci. 35 (5), 774–783.

Boccaletti, G., Ferrari, R., Fox-Kemper, B., 2007. Mixed layer instabilities and restratification. J. Phys. Oceanogr. 37 (9), 2228–2250.

Buckingham, C.E., Naveira Garabato, A.C., Thompson, A.F., Brannigan, L., Lazar, A., Marshall, D.P., George Nurser, A.J., Damerell, G., Heywood, K.J., Belcher, S.E., 2016. Seasonality of submesoscale flows in the ocean surface boundary layer. Geophys. Res. Lett. 43, 2118–2126. https://doi.org/10.1002/2016GL068009.

Callies, J., Ferrari, R., 2013. Interpreting energy and tracer spectra of upper-ocean turbulence in the submesoscale range (1–200 km). J. Phys. Oceanogr. 43 (11), 2456–2474.

Callies, J., Ferrari, R., Klymak, J.M., Gula, J., 2015. Seasonality in submesoscale turbulence. Nat. Commun. 6, 6862. https://doi.org/10.1038/ncomms7862.

Capet, X., McWilliams, J.C., Molemaker, M.J., Shchepetkin, A., 2008a. Mesoscale to submesoscale transition in the California Current System. Part I: Flow structure, eddy flux, and observational tests. J. Phys. Oceanogr. 38 (1), 29–43.

Capet, X., McWilliams, J.C., Molemaker, M.J., Shchepetkin, A., 2008b. Mesoscale to submesoscale transition in the California Current System. Part II: Frontal Processes. J. Phys. Oceanogr. 38 (1), 44–64.

Charney, J.G., 1971. Geostrophic turbulence. J. Atmos. Sci. 28, 1087–1095.

D'Asaro, E.A., 1978. Mixed layer velocities induced by internal waves. J. Geophys. Res. 83, 2437–2438.

Dong, J., Zhong, Y., 2018. The spatiotemporal features of submesoscale processes in the northeastern South China Sea. Acta Oceanol. Sin. 37, 8–18.

ECMWF, 2011. ECMWF's Operational Model Analysis, starting in 2011. Research Data Archive at the National Center for Atmospheric Research, Computational and Information Systems Laboratory, Boulder CO,. https://doi.org/10.5065/D6ZG6Q9F.

Fang, G., Fang, W., Fang, Y., Wang, K., 1998. A survey of studies on the South China Sea upper ocean circulation. Acta Oceanogr. Taiwan. 37, 1–16.

Fang, G., Wang, G., Fang, Y., Fang, W., 2012. A review on the South China Sea western boundary current. Acta Oceanol. Sin. 31, 1–10.

Ferrari, R., Wunsch, C., 2009. Ocean circulation kinetic energy: Reservoirs, sources, and sinks. Annu. Rev. Fluid. Mech. 41 (1), 253–282.

Gan, J., Li, H., Curchitser, E.N., Haidvogel, D.B., 2006. Modeling South China Sea circulation: Response to seasonal forcing regimes. J. Geophys. Res. Oceans. 111 (C6). https://doi.org/10.1029/2005JC003298.

Garrett, C., Munk, W., 1972. Space-time scales of internal waves. Geophys. Fluid Dyn. 3 (1), 225–264. https://doi.org/10.1080/03091927208236082.

Gula, J., Molemaker, M.J., McWilliams, J.C., 2016. Topographic generation of submesoscale centrifugal instability and energy dissipation. Nat. Commun. 7, 12811. https://doi.org/10.1038/ncomms12811.

Haine, T.W.N., Marshall, J., 1998. Gravitational, symmetric, and baroclinic instability of the ocean mixed layer. J. Phys. Oceanogr. 28 (4), 634–658.

Hu, J., Kawamura, H., Hong, H., Qi, Y., 2000. A Review on the Currents in the South China Sea: Seasonal Circulation, South China Sea Warm Current and Kuroshio Intrusion. J. Oceanogr. 56, 607–624.

Klein, P., Hua, B.L., Lapeyre, G., Capet, X., Le Gentil, S., Sasaki, H., 2008. Upper ocean turbulence from high-resolution 3D simulations. J. Phys. Oceanogr. 38, 1748–1763.

Lahaye, N., Gula, J., Roullet, G., 2019. Sea surface signature of internal tides. Geophys. Res. Lett. 46. https://doi.org/10.1029/2018GL081848.

Lapeyre, G., Klein, P., 2006. Dynamics of the upper oceanic layers in terms of surface quasigeostrophy theory. J. Phys. Oceanogr. 36 (2), 165–176.

Large, W.G., Yeager, S.G., 2004. Diurnal to decadal global forcing for ocean and sea-ice models: The data sets and flux climatologies, NCAR Tech. Note NCAR/TN-460 + STR pp 105, Boulder, Colo. Natl. Cent. for Atmos. Res.

Large, W.G., Nurser, A.J.G., 2001. Ocean surface water mass transformation. In: Siedler, G., Church, J., Gould, J. (Eds.), Ocean Circulation and Climate. Academic Press, San Diego, Calif., pp. 317–336.

Le Traon, P.-Y., Klein, P., Hua, B.L., Dibarboure, G., 2008. Do altimeter wavenumber spectra agree with the interior or surface quasigeostrophic theory? J. Phys. Oceanogr. 38 (5), 1137–1142.

Li, J., Dong, J., Yang, Q., Zhang, X., 2019. Spatial-temporal variability of submesoscale currents in the South China Sea. J. Oceanol. Limnol. 37, 474–485.

Liu, F., Tang, S., Chen, C., 2015. Satellite observations of the small-scale cyclonic eddies in the western South China Sea. Biogeosciences 12, 299–305.

Liu, G., He, Y., Shen, H., Qiu, Z., 2010. Submesoscale activity over the shelf of the northern South China Sea in summer: simulation with an embedded model. Chin. J. Oceanol. Limnol. 28, 1073–1079.

Mahadevan, A., Tandon, A., 2006. An analysis of mechanisms for submesoscale vertical motion at ocean fronts. Ocean Model. 14 (3–4), 241–256.

Mahadevan, A., 2016. Impact of submesoscale physics on primary productivity of plankton. Annu. Rev. Mar. Sci. 8(1), 17.1–17.24.

Mahadevan, A., 2019. Submesoscale Processes. In Cochran, J.K., Bokuniewicz, H.J., Yager, P.L. (Ed.), Encyclopedia of Ocean Sciences. Academic Press, 3rd Edition, pp 35–41.

Marshall, J., Adcroft, A., Hill, C., Perelman, L., Heisey, C., 1997. A finite-volume, incompressible Navier Stokes model for studies of the ocean on parallel computers. J. Geophys. Res. 102, 5753–5766.

McWilliams, J.C., 2016. Submesoscale currents in the ocean. Proc. R. Soc. A. 472, 20160117. https://doi.org/10.1098/rspa.2016.0117.

Munk, W., Armi, L., Fischer, K., Zachariasen, Z., 2000. Spirals on the sea. Proc. Roy. Soc. London A. 456, 1217–1280.

Pawlowicz, R., Beardsley, B., Lentz, S., 2002. Classical tidal harmonic analysis including error estimates in MATLAB using T TIDE. Comput. Geosci. 28, 929–937.

Qiu, B., Chen, S., Klein, P., Sasaki, H., Sasai, Y., 2014. Seasonal mesoscale and submesoscale eddy variability along the North Pacific Subtropical Countercurrent. J. Phys. Oceanogr. 44, 3079–3098.

Richman, J.G., Arbic, B.K., Shriver, J.F., Metzger, E.J., Wallcraft, A.J., 2012. Inferring dynamics from the wavenumber spectra of an eddying global ocean model with embedded tides. J. Geophys. Res. Oceans. 117 (C12). https://doi.org/10.1029/2012JC008364.

Rocha, C.B., Chereskin, T.K., Gille, S.T., Menemenlis, D., 2016a. Mesoscale to submesoscale wavenumber spectra in Drake Passage. J. Phys. Oceanogr. 46 (2), 601–620.

Rocha, C.B., Gille, S.T., Chereskin, T.K., Menemenlis, D., 2016b. Seasonality of submesoscale dynamics in the Kuroshio Extension. Geophys. Res. Lett. 43, 11304–11311. https://doi.org/10.1002/2016GL071349.

Rudnick, D., 2001. On the skewness of vorticity in the upper ocean. Geophys. Res. Lett. 28, 2045–2048. https://doi.org/10.1029/2000GL012265.

Sasaki, H., Klein, P., 2012. SSH wavenumber spectra in the North Pacific from a high-resolution realistic simulation. J. Phys. Oceanogr. 42 (7), 1233–1241.

Shaw, P.-T., Chao, S.-Y., 1994. Surface circulation in the South China Sea. Deep Sea Res. Part I. 41 (11), 1663–1683.

Stammer, D., 1997. Global characteristics of ocean variability estimated from regional TOPEX/POSEIDON altimeter measurements. J. Phys. Oceanogr. 27 (8), 1743–1769.

Stammer, D., Ueyoshi, K., Köhl, A., Large, W.G., Josey, S.A., Wunsch, C., 2004. Estimating air-sea fluxes of heat, freshwater, and momentum through global ocean data assimilation. J. Geophys. Res. Oceans. 109, C05023. https://doi.org/10.1029/2003JC002082.

Thomas, L.N., Tandon, A., Mahadevan, A., 2008. Submesoscale processes and dynamics. In: Hecht, M.W., Hasumi, H. (Ed.), Ocean Modeling in an Eddying Regime, Geophys. Monogr. Vol. 177, Am. Geophys. Union., Washington, D.C., pp. 17–38.

Thomas, L.N., Taylor, J.R., Ferrari, R., Joyce, T.M., 2013. Symmetric instability in the Gulf Stream. Deep Sea Res. Part II. 91, 96–110.

Timmermans, M.-L., Winsor, P., 2013. Scales of horizontal density structure in the Chukchi Sea surface layer. Cont. Shelf Res. 52, 39–45.

Torres, H.S., Klein, P., Siegelman, L., Qiu, B., Chen, S., Ubelmann, C., Wang, J., Menemenlis, D., Fu, L.-L., 2019. Diagnosing ocean-wave-turbulence interactions from space. Geophys. Res. Lett. 46. https://doi.org/10.1029/2019GL083675.

Verma, V., Pham, H.T., Sarkar, S., 2019. The submesoscale, the finescale and their interaction at a mixed layer front. Ocean Model. 140, 101400. https://doi.org/10.1016/j.ocemod.2019.05.004.

Wang, D.-P., Flagg, C.N., Donohue, K., Rossby, H.T., 2010. Wavenumber spectrum in the Gulf Stream from shipboard ADCP observations and comparison with altimetry measurements. J. Phys. Oceanogr. 40 (4), 840–844.

Whitt, D.B., Thomas, L.N., 2015. Resonant generation and energetics of wind-forced near-inertial motions in a geostrophic flow. J. Phys. Oceanogr. 45, 181–208.

Xu, Z., Liu, K., Yin, B., Zhao, Z., Wang, Y., Li, Q., 2016. Long-range propagation and associated variability of internal tides in the South China Sea. J. Geophys. Res. Oceans. 121, 8268–8286.

Yu, J., Zheng, Q., Jing, Z., Qi, Y., Zhang, S., Xie, L., 2018. Satellite observations of submesoscale vortex trains in the western boundary of the South China Sea. J. Mar. Syst. 183, 56–62.

Zhao, R., Zhu, X.-H., 2016. Weakest winter South China Sea western boundary current caused by the 2015–2016 El Niño event. J. Geophys. Res. Oceans. 121, 7673–7682.

Zhao, Z., Wang, J., Menemenlis, D., Fu, L.-L., Chen, S., Qiu, B., 2019. Decomposition of the multimodal multidirectional M_2 internal tide field. J. Atmos. Oceanic Technol. 36, 1157–1173.

Zhong, Y., Bracco, A., Tian, J., Dong, J., Zhao, W., Zhang, Z., 2017. Observed and simulated submesoscale vertical pump of an anticyclonic eddy in the South China Sea. Sci. Rep. 7, 44011. https://doi.org/10.1038/srep44011.

Zu, T., Gan, J., Erofeeva, S.Y., 2008. Numerical study of the tide and tidal dynamics in the South China Sea. Deep Sea Res. Part I. 55, 137–154.

Zu, T., Xue, H., Wang, D., Geng, B., Zeng, L., Liu, Q., Chen, J., He, Y., 2019. Interannual variation of the South China Sea circulation during winter: intensified in the southern basin. Clim. Dynam. 52, 1917–1933.